MATERIALS CHEMISTRY FRONTIERS

REVIEW

View Article Online
View Journal | View Issue

Cite this: *Mater. Chem. Front.*, 2024, **8**, 903

Recent advances in metal-based electrocatalysts: from fundamentals and structural regulations to applications in anion-exchange membrane fuel cells

Ali Han[a] and Gang Liu *[ab]

Alkaline exchange membrane fuel cells (AEMFCs) have broad application prospects due to the use of low-cost, non-precious catalysts. Furthermore, a wide range of fuels, for example, carbon-neutral hydrogen (H_2) and ammonia (NH_3), can be directly used in H_2-fueled AEMFCs and NH_3-fueled AEM direct ammonia fuel cells (AEM-DAFCs). However, the development of the above-mentioned AEMFCs is hindered by the sluggish dynamics of the alkaline hydrogen oxidation reaction (HOR), ammonium oxidation reaction (AOR), and oxygen reduction reaction (ORR) and low efficiency catalysts for these electrode reactions. Thus, it is expected that the rational design and controlled synthesis of highly efficient, durable catalysts will enable AEMFCs to achieve comparable performance to or even a higher performance than that of proton exchange membrane fuel cells (PEMFCs), which usually require high-cost platinum group metals (PGMs). In particular, the proposed catalytic mechanism of these reactions in alkaline media is still under debate, especially of the HOR and AOR. Herein, we present an in-depth, comprehensive understanding of the alkaline HOR, AOR, and ORR based on metal catalysts, especially employing PGM-free catalysts, including the proposed mechanisms and the current development of catalysts and AEMFCs. Finally, we highlight the prevailing challenge of the mechanisms and catalysts for each reaction and outline the possible development directions for AEMFCs. We anticipate that this review will offer global scientific insights and a roadmap for the design of catalysts for alkaline electrode reactions to accelerate the further development of AEMFC technology.

Received 8th September 2023,
Accepted 10th November 2023

DOI: 10.1039/d3qm00947e

rsc.li/frontiers-materials

[a] *Shenyang National Laboratory for Materials Science, Institute of Metal Research, Chinese Academy of Sciences, 72 Wenhua Road, Shenyang, 110016, China. E-mail: gangliu@imr.ac.cn*
[b] *School of Materials Science and Engineering, University of Science and Technology of China, 72 Wenhua Road, Shenyang 110016, China*

1. Introduction

Hydrogen (H_2) is a very promising, sustainable clean fuel as it only generates water when consumed in a fuel cell. However, to

Ali Han

Ali Han received her PhD from the School of Chemistry and Materials Science, University of Science and Technology of China (USTC) in 2016. She worked as a Postdoctoral Researcher at King Abdullah University of Science and Technology (KAUST) and Tsinghua University. Currently, she is a Professor of IMR, CAS. Her current research interests focus on the design of low-cost and effective electrocatalysts and devices for fuel cells.

Gang Liu

Gang Liu is a Professor and the Director of IMR, CAS. He received his Bachelor's Degree in Materials Physics from Jilin University in 2003 and PhD in Materials Science from IMR in 2009. His main research interest focuses on energy conversion materials and devices for fuels.

realize its commercial utilization, technical barriers pertaining to its transportation, storage, and distribution need to be urgently resolved. Thus, to address these complications and achieve a hydrogen economy, the utilization of hydrogen carriers has been proposed. Among the candidates for energy carriers, ammonia (NH_3) is promising because it is a popular commodity chemical and is stored, transported, and used worldwide.[1,2] In contrast, the H_2 network is underdeveloped. Additionally, the NH_3 economy has also attracted attention due to the following advantages: (1) easy storage and transportation, (2) a high volumetric energy density, (3) low-cost H_2 carriers and a zero-carbon fuel; and (4) non-flammability. However, the main concern associated with NH_3 is its high toxicity compared to other types of energy sources; however, it can be detected by the human nose at concentrations as low as 1 ppm, allowing precautions to be taken in the event of a leak or spill. Hence, H_2/NH_3-powered fuel cells are considered extremely promising energy conversion devices for mobile and stationary applications due to their great potential to be affordable, energy dense, and carbon neutral.

Generally, NH_3 can be directly utilized in direct ammonia fuel cells (DAFCs) or by supplying H_2 to H_2-realated fuel cells *via* thermal decomposition for low temperature alkaline exchange membrane fuel cells (AEMFCs).[3,4] The major distinction between H_2- and NH_3-powered FCs is that H_2 can be used as anode fuels in an alkaline environment for AEMFCs and in acidic conditions for proton-exchange membrane fuel cells (PEMFCs), while NH_3 can only power AEM-DAFCs in alkaline media because only molecular NH_3 can be oxidized at the anode side besides the ammonium cation (NH_4^+). Fortunately, non-precious catalysts can be used at both the anode and cathode sides in less harsh alkaline operating conditions, which is superior to PEMFCs, where almost only platinum group metals (PGMs) can efficiently work on both electrode sides in harsh acid media. Moreover, PEMFCs require perfluorinated membranes and high acid-tolerance stack hardware, resulting in extremely high cost. Thereby, AEMFCs are potentially low-cost alternatives to PEMFCs due to the use of less costly non-precious catalysts, alkaline membranes and stack hardware.

However, despite their great promise, AEMFCs are severely restrained by the lack of efficient electrocatalysts. In a typical H_2-fueled AEMFC and NH_3-fueled AEM-DAFC (Fig. 1), the same oxygen reduction reaction (ORR, $O_2 + 2H_2O + 4e^- = 4OH^-$) occurs on the cathode side of both cells. Also, the hydrogen oxidation reaction (HOR, $H_2 + 2OH^- = 2H_2O + 2e^-$) and ammonia oxidation reaction (AOR, $2NH_3 + 6OH^- = N_2 + 6H_2O + 6e^-$) occur on the former and latter cells, respectively. To data, PGM-free ORR catalysts have been intensively investigated, including transition metal oxides,[5,6] metal-embedded nitrogen-doped carbon (M–N–C)[7–10] and even metal-free catalysts,[11] which are anticipated to facilitate the fast development of AEMFC technology. However, there is a lack of efficient non-precious catalysts for the HOR and AOR. Hence, the prevailing challenge mainly comes from the anode side of alkaline HOR and AOR, in which PGMs still deliver the best HOR/AOR performance.[12–18]

Previous reports have demonstrated that the alkaline HOR activity is usually 2 orders of magnitude lower compared with that in the acid media, which requires higher loadings of PGMs to achieve the desired high performance for commercial applications and further increases the cost of AEMFCs.[19,20] Thus, the HOR is the limiting reaction requiring more active PGM-free catalysts than Pt. Recently, Ni-based catalysts have been widely explored to exhibit the most active HOR performance among the PGM-free HOR alternatives.[21–25] However, Ni metal is easily oxidized under the operating conditions, leading to the generation of inescapable oxide species, which lower the activity. In this regard, research on the HOR mechanisms and activity descriptors in alkaline media can rationally guide the design for the development of high-efficient Ni-based HOR catalysts.

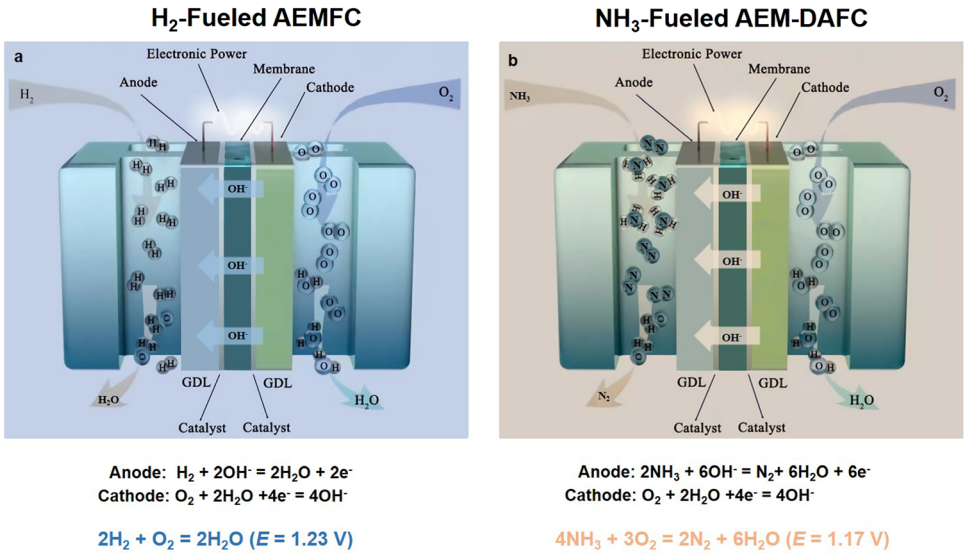

Fig. 1 A schematic view of the components and working principles of an H_2-fueled AEMFC (a) and NH_3-fueled AEM-DAFC (b).

The development of DAFCs is still in its infancy compared with H_2-fueled fuel cells. This is mainly attributed to the more complex and sluggish $6e^-$ process of the AOR than the $2e^-$ process of the HOR. To date, AOR electrocatalysts are mainly focused on PGMs. Also, the overpotentials of Pt-related electrocatalysts are universally larger than 0.40 V, which severely lowers the energy conversion efficiency of DAFCs. Thus, herein, we focus our discussion on the recent developments in the AOR catalytic mechanism, AOR catalysts and DAFC technologies. It is worth noting that only low-temperature DAFCs will be discussed due to their rapid start-up compared with high-temperature DAFCs, for example, ammonia-fueled solid oxide fuel cells (SOFCs).

Recently, AEMFCs have aroused increasing interest. Accordingly, numerous reviews have been reported on this topic, with most focusing on the specific topic of H_2-powered AEMFCs.[4,26] In contrast, NH_3-powered AEM-DAFCs have rarely been discussed to date. Particularly, an overview covering the recent developments in HOR/AOR/ORR catalysts has not been reported. Thus, in this review, firstly we introduce the fundaments of H_2-fueled AEMFCs and NH_3-fueled AEM-DAFCs. Then, we discuss the underlying catalytic mechanisms in the three main reactions (HOR, AOR and ORR) and corresponding recent progress in catalysts. In the case of HOR catalysts, Ni-related metal catalysts are mainly discussed because of their excellent intrinsic activity for the HOR and great promise for practical applications. Also, AOR catalysts are generally classified into three types, including molecular catalysts, PGM-related catalysts and PGM-free catalysts. Regarding ORR catalysts, the metal-related catalysts are based on pyrolyzed carbon-based catalysts, pyrolysis-free catalysts and metal oxide and related hybrid catalysts. Finally, the future challenges and perspectives for AEMFCs are proposed, including advanced catalyst screening, exploring mechanisms, high-performance membrane electrode assembly (MEA) and technical obstacles. To the best of our knowledge, this is the first review that attempts to summarize the development of HOR, AOR and ORR catalysts in alkaline media with a focus on low-temperature AEMFCs.

2. Fundamentals

Typically, AEMs are susceptible to CO_2 in air; however, unlike alkaline fuel cells (AFCs), precipitates such as K_2CO_3 and Na_2CO_3 are not formed in AEMFC systems. Nevertheless, CO_2 reacts with OH^- to generate CO_3^{2-} ions. In this case, the presence of CO_3^{2-} ions is still a challenging problem due to their much lower conductivity than OH^-, further reducing the whole conductivity of the AEM and increasing the electrolyte resistance, thereby degrading the fuel cell performance. Thus, the development of AEMs with excellent chemical stability, high OH^- conductivity and stable mechanical properties is crucial to realize long-term durability in AEMFCs. Pure O_2 or CO_2-free air often serve as an oxidant to bypass the generation of CO_3^{2-} ions. In this review, the choice of AEM and electrolyte for AEMFCs will not be discussed given that reviews on the properties of AEM have been intensively documented.[3,4,27–30]

2.1. Fundamental principles of H_2-fueled AEMFCs

H_2 is an ideal renewable energy with a high energy density (120–140 MJ kg^{-1}), great sustainability and zero emissions. However, an H_2 economy cannot be achieved until the related technical barriers such as the transportation, storage and distribution of H_2 are addressed. An important component of a single AEMFC is the membrane electrode assembly (MEA), involving the catalyst layer (anode HOR/cathode ORR electrodes), AEM and gas diffusion layer (GDL), as shown in Fig. 1a. The polymer AEM serves to divide the electrodes and selectively transport OH^- ions from the cathode side to the anode side. The theoretical cell voltage for the overall reaction of a single AEMFC is 1.23 V at 25 °C (eqn (2.1)–(2.3)). However, the practical cell voltage is less than 1.23 V due to the irreversible fuel crossover, ohmic drop and polarization. The former two aspects can be advanced by the engineering approach, while the latter is related to the kinetics of the electrode reaction processes. Generally, the property and cost of membrane electrodes determine the cell performance (cell voltage, durability and total cost) of AEMFCs. Currently, decelerating the voltage loss from the viewpoint of electrochemical fundamentals is a hot topic. For example, enhancing the intrinsic activity of catalysts and the mass transfer process of H_2/H_2O. Generally, the kinetic parameters are obtained by rotating disk electrode (RDE) testing systems to avoid the effect of other factors. Hence, most of the mechanism studies on the half reaction (*e.g.*, HOR and ORR) are based on the RDE system and the HOR/ORR mechanism can further rationally guide the exploration of efficient catalysts with high AEMFC performance.

H_2-fuelded AEMFCs:

$$\text{Anode: } H_2 + 2OH^- \rightarrow 2H_2O + 2e^-,\ E^0 = -0.83\ \text{V} \quad (2.1)$$

$$\text{Cathode: } O_2 + 2H_2O + 4e^- \rightarrow 4OH^-,\ E^0 = 0.40\ \text{V} \quad (2.2)$$

$$\text{Overall reaction: } O_2 + 2H_2 \rightarrow 2H_2O,\ E^0 = 1.23\ \text{V} \quad (2.3)$$

2.2. Fundamental principles of NH_3-fueled-AEM-DAFCs

NH_3-powered fuel cells are regarded as either direct or indirect, largely depending on where NH_3 decomposition occurs. The route of NH_3 decomposition for on-site H_2 production has been previously reviewed.[31] However, DAFCs have the benefits of directly using NH_3 in the fuel cell and utilizing the chemical energy stored by NH_3. This not only eliminates the need for onboard H_2 storage and evades the decomposition of NH_3, but also reduces the facility and operating costs.

DAFCs can be classified according to their electrolyte, temperature, *etc.* Typically, according to the electrolyte used, DAFC technologies can be summarized as the following types:

- Oxygen anion conducting electrolyte-based solid oxide fuel cells (SOFC-O),[32]
- Proton-conducting electrolyte-based solid oxide fuel cells (SOFC-H),[33]
- Alkaline ammonia fuel cells (AAFCs) (including molten hydroxide ammonia fuel cells),[34]
- Microbial ammonia fuel cells (MAFCs)[35,36] and

• Alkaline membrane-based fuel cells (AMFCs).[37,38]

Typically, NH_3-fueled-SOFCs require a high operating temperature to accelerate the decomposition of NH_3 at the anode side, which needs solid oxide electrolytes with PEM, AEM or molten hydroxides.[32,39] When a PEM is used, the anode side reaction is: $2NH_3 \rightarrow 3H_2 + N_2$; $H_2 \rightarrow 2H^+ + 2e^-$, while when an AEM is used, the anode side reaction is: $2NH_3 \rightarrow 3H_2 + N_2$; $H_2 + O^{2-} \rightarrow 2H_2O + 2e^-$. This type of system has shown great promise due to its high energy conversion efficiency, environmentally friendly nature, good fuel flexibility and good performance when H_2 is used as the fuel. However, for its practical application, several issues must be addressed, including the simultaneous formation of N_2 to dilute H_2 at the anode side and the corresponding formation of NO_x^- if N_2 reacts with oxygen species at high temperature.

The earliest type of AAFC was invented by Cairns *et al.* in 1968, using a KOH electrolyte to power the device at the operating temperature in the range of 50–200 °C.[40] Inspired by this work, extensive research has been conducted using molten hydroxide electrolytes for DAFCs.[34,41,42] However, the durable performance of this type of fuel cell remains challenging because the strong reaction between CO_2 (from the air) and hydroxide electrolytes leads to the generation of carbonate ions such as K_2CO_3, which precipitate, lower the overall conductivity, and eventually poison the battery.

MAFCs are also alternative technology, which have gained attention due to their ability to process NH_3-contaminated wastewater, while simultaneously producing electricity. Generally, MAFC technology utilizes microorganisms to convert chemical energy from biodegradable materials into electricity.[35,36] The DAFCs presented here are mainly the AEM-DAFC type, which utilize aqueous alkaline media according to a similar principle as AAFCs, give that they also operate by transferring OH^- ions and work at a relatively low temperature of 50–120 °C.[37,38] Unlike NH_3-fueled-SOFCs, H_2 does not participate in the anode reaction. Instead, H_2O serves as an intermediate substance with the generated electric current, following eqn (2.4).

As shown in Fig. 1, in both fuel cells, O_2 molecules are reduced to OH^- at the cathode, and then reach the anode side *via* the AEM. In the case of the anode area in H_2-fueled AEMFCs, H_2 molecules are anodized and combined with OH^- to form H_2O, while NH_3 molecules are oxidized and combined with OH^- to form N_2 in NH_3-fueled DAFCs. Ultimately, an external circuit is formed by the electrons produced from the redox reactions on both sides of the electrode and powers the required devices. The thermodynamic voltage of NH_3-fueled DAFCs is 1.17 V (298 K). Similar to H_2-fueled AEMFC, the cell voltage of NH_3-fueled DAFCs often needs to overcome the slow electrode dynamics and the inevitable internal ohmic resistances.

The device of AEM-DAFCs is assembled by coupling the anodic AOR *via* a 6e- reaction process in alkaline aqueous solution:

$$\text{Anode: } 2NH_2 + 6OH^- \rightarrow N_2 + 6H_2O + 6e^-,\ E^0 = -0.77\ \text{V} \quad (2.4)$$

$$\text{Cathode: } O_2 + 2H_2O + 4e^- \rightarrow 4OH^-,\ E^0 = -0.40\ \text{V} \quad (2.2)$$

$$\text{Overall reaction: } 4NH_3 + 3O_2 \rightarrow 2N_2 + 6H_2O,\ E^0 = 1.17\ \text{V} \quad (2.5)$$

3. Hydrogen oxidation reaction (HOR)

3.1. Mechanism understanding of HOR

HOR is the limiting reaction in H_2-fueled AEMFCs. In particular, Pt shows higher activity in HOR in acid media, whereas much slower activity in alkaline. Hence, it is a prerequisite to have deep insight into the HOR mechanism. Unlike HOR in acidic media, involving only protons, the alkaline HOR involves the formation of water. HOR in alkaline media follows three elementary steps, as follows:

$$\text{Tafel step: } H_2 + 2* \rightarrow 2H_{ad} \quad (3.1)$$

$$\text{Heyrovsky step: } H_2 + OH^- + * \rightarrow H_{ad} + H_2O + e^- \quad (3.2)$$

$$\text{Volmer step: } H_{ad} + OH^- \rightarrow H_2O + e^- + * \quad (3.3)$$

$$\text{Total reaction: } H_2 + 2OH^- \rightarrow 2H_2O + 2e^-$$

where * represents the active site and H_{ad} refers to the adsorbed H atoms.

Four mechanisms are involved in HOR according to the rate-determining step (RDS). The kinetic expressions and Tafel slopes (TSs) are discussed in the following sections.

Volmer (RDS)–Tafel mechanism. In this mechanism, the Volmer step is the RDS and HOR exhibits the absolute TS value of 118 mV dec^{-1}, indicating a symmetric figure in the following Butler–Volmer (BV) fitting (3.4).

$$i = 2i_0\left[e^{\frac{-\alpha F}{RT}\eta} + e^{\frac{\beta F}{RT}\eta}\right](\alpha = \beta = 0.5) \quad (3.4)$$

where i_0 represents the exchange current.

Volmer–Tafel (RDS) mechanism. In the Volmer–Tafel (RDS) mechanism, the Tafel step is the RDS. However, the kinetics does not abide by the BV equation because the Tafel step does not involve charge transfer. Hence, HOR exhibits the absolute TS value of 30 mV dec^{-1} according to the B-V fitting (3.5), as follows:

$$\eta = \frac{RT}{2F}\ln\left(1 + \frac{i}{i_T}\right) \quad (3.5)$$

Volmer (RDS)–Heyrovsky mechanism. In the Volmer (RDS)–Heyrovsky mechanism, the Volmer step is the RDS. HOR exhibits the absolute TS value of 39 mV dec^{-1} according to the B–V fitting (3.6), as follows:

$$i = 2i_0\left[e^{\frac{-\alpha F}{RT}\eta} + e^{\frac{(1+\beta)F}{RT}\eta}\right](\alpha = \beta = 0.5) \quad (3.6)$$

Volmer–Heyrovsky (RDS) mechanism. In the Volmer–Heyrovsky (RDS) mechanism, the Heyrovsky step is the RDS. HOR

exhibits the absolute TS value of 118 mV dec^{-1} according to the B-V fitting (3.7), as follows.

$$i = 2i_0\left[e^{\frac{-(1+\alpha)F}{RT}\eta} + e^{\frac{\beta F}{RT}\eta}\right](\alpha = \beta = 0.5) \qquad (3.7)$$

Notably, for the Volmer (RDS)–Tafel and Volmer–Heyrovsky (RDS) mechanisms, the Tafel slope has the same value (118 mV dec^{-1}), which makes it difficult to distinguish them. In addition, within the experimental uncertainty, the Tafel slope of the Volmer–Tafel (RDS) (30 mV dec^{-1}) and Volmer (RDS)–Heyrovsky (39 mV dec^{-1}) mechanisms is very close, which makes it difficult to draw conclusions of exclusivity to identify the specific reaction mechanism. Thereby, it is significant to employ other analytical methods to verify the HOR mechanism. The activity descriptor of HOR has been widely reviewed elsewhere,[4,43–46] and hence it will not be highlighted here.

3.2. Recent electrocatalysts for HOR

PGM-related materials have been demonstrated to show efficient HOR performances in alkaline electrolyte, especially Pt and Ir.[47] However, the anode HOR activity of PGM catalysts is much slower in alkaline media than that in acid media (2–3 orders of magnitude).[20,48] Thus, to obtain the desired AEMFC performance, the anode requires higher PGM loadings, offsetting the cost reduction of utilizing a PGM-free cathode. Hence, we mainly introduce the durable PGM-free HOR catalysts in this part to improve the eventual commercial development of H_2-fueled AEMFC technology. In the case of PGM-free HOR catalysts, only Ni-based catalysts have shown comparable HOR activity to Pt/C in alkaline media. Table 1 presents the HOR performance of PGM-free catalysts measured in alkaline electrolyte. Recently, increasing research advances have shown that in alkaline media, the typical HOR processes follow the Tafel–Volmer or Heyrovsky–Volmer mechanism.[49]

3.2.1. Ni–N-related inorganic compounds. Yan *et al.* reported that nitrogen-doped carbon nanotube-supported Ni nanoparticles (NPs) showed HOR activity in alkaline media; however, their performance was still inferior to Pt catalysts.[50] Moreover, due to the relatively strong binding affinity of Ni to oxygen, they suffered from low stability at potentials above 0.1 V *vs.* RHE, thereby seriously blocking their active sites. Thus, to obtain the required power output, HOR catalysts should work at potentials greater than 0.3 V relative to RHE.[51] Recently, the investigated Ni–N-related catalysts are typically nickel nitrides or N-doped Ni-based catalysts, which have been intensively investigated to exhibit superior HOR activity compared to pure Ni species. The calculated results have demonstrated that introducing N heteroatoms can significantly enhance the HOR activity due to the optimal value of ΔG_H ($\sim$0) and decrease the activation energies of water formation and water dissociation. For example, Hu *et al.* reported the development of Ni_3N/C as an efficient HOR catalyst with superior HOR activity and stability compared to Ni.[22] It was revealed that the Ni d band shifted down from Ni to Ni_3N and the interfacial charge shifted from Ni_3N to C, thereby weakening the hydrogen binding energy (HBE) and OH binding energy (OHBE), and enhancing the activity and stability of HOR. Recently, Wu *et al.* fabricated Mo-modified Ni_3N, which delivered much higher activity than pure Ni_3N for HOR.[52] The MoO_2 and MoO_4^{2-} species were detected by *operando* Raman spectroscopy in the potential range of -0.2 V to 0.2 V *vs.* RHE. Also, these Mo-related species could significantly enhance the HOR catalytic performance by the weakened HBE and strengthened OHBE based on the bi-functional mechanism. Wang *et al.* reported that N-inserted Ni nanosheets exhibited enhanced HOR activity in alkaline media.[53] The mechanistic results demonstrated that N insertion in the Ni lattices could induce strong d-sp orbital hybridization, which could further facilitate the optimal adsorption of hydrogen intermediates. In addition, the surface strain derived from the lack of Ni–Ni coordination also enhanced the adsorption of OH species. The eventual modulation of the adsorption behaviors of the H and OH species significantly promoted the rate-determining Volmer step and triggered an excellent HOR performance. Later, they developed Ni-vacancy-rich Ni_3N (Ni_3N-r) as a platform for the arrangement of the Ni active center electrons in HOR.[54] Compared to the Ni_3N-vacancy-poor (Ni_3N-p) sample, the Ni ds-N 2p valence-electron-orbital interaction in the Ni_3N-r sample dramatically increased, thereby broadening the Ni ds valence-electron orbitals around the Ni vacancies in the Ni_3N-r

Table 1 A summary of the reported HOR catalytic performances of various PGM-free-related HOR catalysts measured in alkaline electrolytes

HOR catalysts	j_0, ECSA (μA cm^{-2})	j_k, Disk (mA cm^{-2})	j_{m0} (A g^{-1})	j_{mk} (A g^{-1})@50 mV	Ref.
Ni/V_2O_3	38	—	—	42.1	*Angew. Chem., Int. Ed.* 2023, **62**, e202217275.[21]
Ni_3N	80.08	11.09	—	—	*Nano Lett.* 2023, **23**, 107–115[159]
Ni-H_2-NH_3	70	4.55		59.2	*Nat. Mater.* 2022. **21**, 804–810.[23]
$Ni_{5.2}WCu_{2.2}$	14	—	2.54	2.55	*Nat. Commun.* 2021, **12**, 2686.[160]
Mo-Ni_3N	1.81	7.3	9.05	36.5	*ACS Appl. Nano Mater.* 2021, **4**, 11473–11479.[52]
Ni_4Mo	65	33.8	—	—	*Nat. Commun.* 2020, **11**, 4789.[60]
Ni-H_2	2.9	5.85	24.41	50.4	*Angew. Chem., Int. Ed.* 2020, **59**, 10797–10801.[161]
CeO_2(r)-Ni/C	38	1.73	—	12.3	*Angew. Chem., Int. Ed.* 2019, **58**, 14179–14183.[25]
Ni/NiO/C	26	1.59	—	5	*Angew. Chem., Int. Ed.* 2019, **58**, 10644–10649.[63]
Ni_3N/C	14	3.89	12.0	24.4	*Angew. Chem., Int. Ed.* 2019, **58**, 7445–7449.[22]
Ni/SC	40.2	1.52	7.4	11.0	*J. Mater. Chem. A*, 2019, **7**, 10936–10941.[162]
Ni/KB	28.6	—	7.0	—	*J. Electroanal. Chem.* 2019, **852**, 113551.[163]
Ni_6Cu_4	34	—	—	—	*ACS Appl. Energy Mater.* 2019, **2**, 3160–3165.[164]

sample. Moreover, the integrated crystal orbital Hamiltonian population (COHP) of the Ni_{AC} ds-O 2p bonds in the Ni_3N-r sample showed an enhanced absolute value, indicating that the strengthened interactions could strengthen the OH binding at the Ni active centers. The weakened H binding and increased OH binding interactions in the Ni_3N-r sample were confirmed by the varying values of HBE and OHBE (Fig. 2a). The well-regulated H/OH binding interactions in the Ni_3N-r sample could notably lower the energy barrier (~0.73 eV), which was much lower than that of the Ni_3N-p (1.144 eV), as shown in Fig. 2b. This work shed new light on exploring HOR catalysts by regulating the electron arrangement of their active sites.

Recently, Hu and co-workers reported that an Ni–H_2–NH_3 HOR catalyst exhibited a record AEMFC performance. The Ni–H_2–NH_3 catalyst and reference catalysts were prepared by pyrolyzing the Ni-MOF at different mixture atmospheres, as shown in Fig. 2c. The choice of atmosphere showed a great influence on the size of the Ni NPs and their HOR performance. As shown in Fig. 2d, the Ni–H_2–NH_3 catalyst exhibited the best HOR activity, which is even comparable with the commercial Pt/C. However, to date, whether OH^- is involved in HOR in alkaline media is still unclear. Thus, to demonstrate whether HBE and OHBE are involved in the present Ni-based catalysts, ultraviolet photoelectron spectroscopy (UPS) was further used to examine the Ni valence state in these three catalysts. The metallic nature of all the Ni samples was confirmed due to the passage of electron bands through the Fermi level (Fig. 2e). According to the *d* band theory, the downward movement of the d-band leads to a weakened adsorption strength. Therefore, the HBE and OHBE of the catalysts followed the order of Ni > Ni–H_2 > Ni–H_2–NH_3 > Ni–H_2. The HBE and OHBE experimental results were further demonstrated by H_2/OH chemisorption and isotope tests in 0.1 M KOD, matching well with the prediction of d-band theory. The correlation of the HOR activities with HBE and OHBE was obtained using the chemisorption binding constant as a proxy, as shown in Fig. 2f and g.

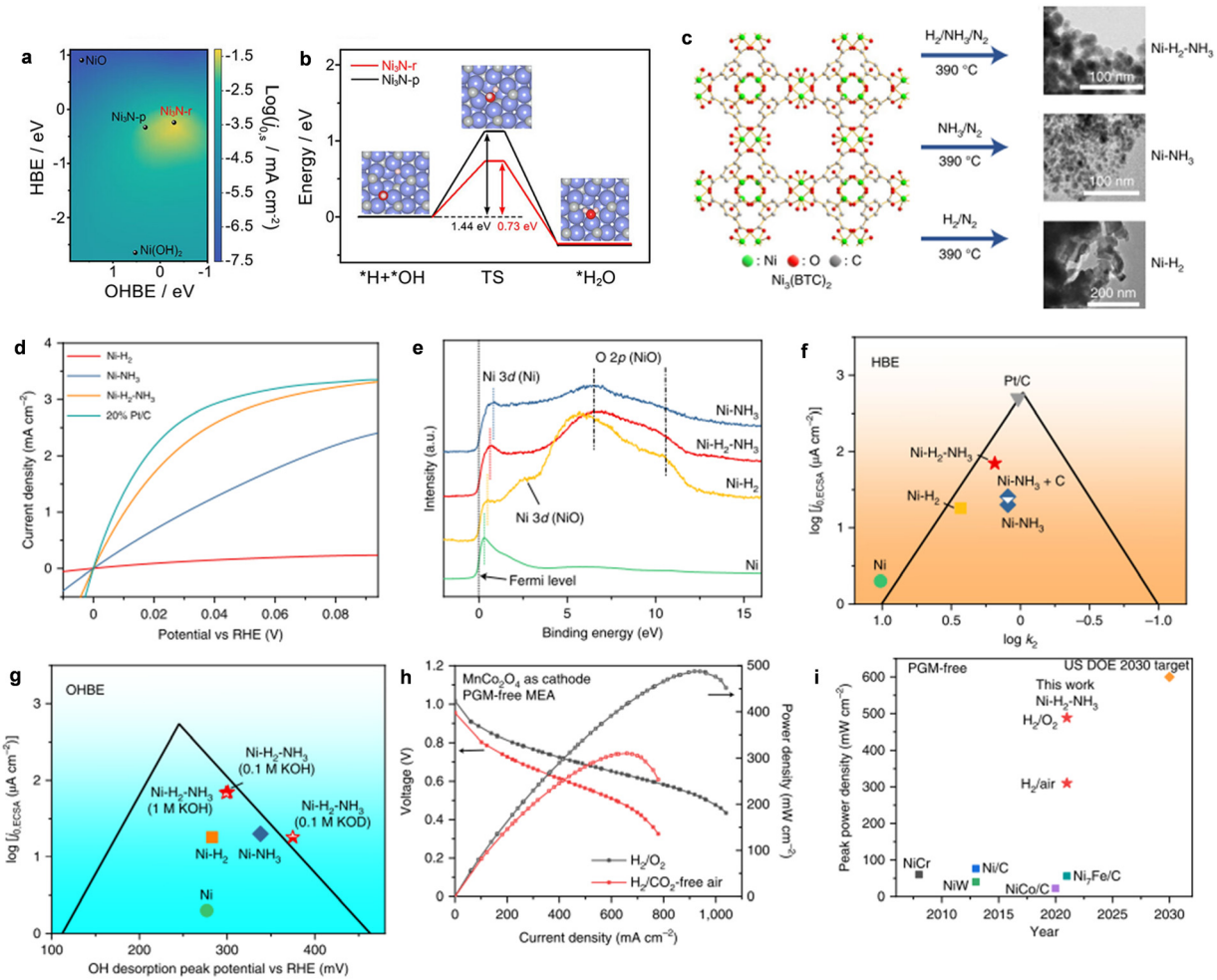

Fig. 2 (a) The logarithm of the HOR activity for different catalysts as a function of HBE and OHBE. (b) The combination of *OH and *H on Ni_3N-p and Ni_3N-r. Reproduced with permission from ref. 54 Copyright 2022, Wiley-VCH GmbH. (c) The synthesis of Ni-based catalysts. (d) HOR polarization curves for different catalysts. (e) UPS spectra analysis. The relationships of studied HOR activities with HBEs (f) and OHBEs (g). (h) The H_2-fueled AEMFC performance using Ni-H_2-NH_3 as the anode and CoMn spinel as the cathode. (i) A comparison of the PGM-free-based peak power density performance. Reproduced with permission from ref. 23 Copyright 2022, Nature Publications.

Based on the predicted HBE theory, it is assumed that the benchmark Pt/C, located at the top of the volcano plot, has the best activity (Fig. 2f), but its performance was inferior to Ni–H_2–NH_3. Hence, the HOR activity was poorly correlated with HBE, indicating that the HOR activity of Ni-based catalysts cannot be explained by a single HBE descriptor. Alternatively, OHBE was represented in OH potential, and the volcano plot is shown in Fig. 2g. Similarly, the HOR activity indicated from the figure was contrary to that predicted by the OHBE theory. However, the experimental results matched well with the combination of HBE and OHBE theory, given that both H_{abs} and OH_{abs} played significant roles in the Volmer step. According to both volcano plots, it could be deduced that the HBE was dominant and the HOR activity followed the order of Ni < Ni–H_2 < Ni–H_2–NH_3. The activity of Ni–NH_3 was much lower than that of Ni–H_2–NH_3 when OHBE was dominant. Hence, the optimal HOR activity for the catalyst was the result of t optimized balance between low HBE and low OHBE. These results further suggested that Ni-based catalysts can be regulated by both the HBE and OHBE theories. Furthermore, Ni–H_2–NH_3 was used as the anodic catalyst in an MEA for the H_2–O_2 AEMFC test, as shown in Fig. 2h. The $CoMn_2O_4$ spinel was employed as the cathode side to integrate a PGM-free MEA. Encouragingly, the H_2–O_2 AEMFC showed a current density of 606 mA cm^{-2} at 0.65 V and a high peak power density of 488 mA cm^{-2}, which is much higher than that of most previously reported PGM-free MEAs (Fig. 2i). A comparison of H_2–O_2 or H_2–air AEMFC performance of PGM-free HOR catalysts is presented in Table 2.

3.2.2. Ni-based metal alloys. It is well-known that amorphous structures exhibit unique physical/chemical properties with short-range ordered and long-range disordered atomic structures, thereby enhancing the catalytic performance of HOR. For example, amorphous NiMo alloy catalysts with different compositions were investigated *via* the electrodeposition technique.[55] The amorphous $Ni_{62}Mo_{38}$ catalysts were found to exhibit the best activity among the investigated catalysts in alkaline media. Additionally, Cu has higher stability against corrosion in alkaline solution and lower cost than Mo/W. Hence, NiCu alloys were further explored, which showed superior HOR activity compared to Ni metals due to the combination of Ni with strong HEB and Cu with weak HBE.[56–58] Similar to the NiCu system, NiAg-based alloys for HOR were also investigated by the combination of experimental results and DFT simulations.[59] The results showed that the Ni-rich $Ni_{0.75}Ag_{0.25}$ possessed the optimal HBE and exhibited much higher stability and activity than pure Ni.

Recently, Yu and co-workers reported the synthesis of $MoNi_4$ and WNi_4 alloys for efficient HOR activity, as shown in Fig. 3a.[60] The polarization curves of $MoNi_4$ and WNi_4 alloys for HOR are shown in Fig. 3b, approaching a zero onset potential for HOR, indicating their remarkable energetics in alkaline media. However, the Ni catalysts showed a negligible HOR performance. Importantly, both catalysts could achieve a diffusion-limiting current in the potential region of >0.05 V and react in the hybrid kinetic-diffusion control region of 0–0.05 V. Moreover, the $MoNi_4$ alloy showed a much lower geometric J_0 of 3.41 mA cm^{-2} (Fig. 3c) than the other catalysts. The *i–t* curves in Fig. 3d further demonstrated the robust stability of both catalysts at the overpotential of 60 mV. DFT calculations were performed on the optimized catalyst modes of $MoNi_4$ (211), WNi_4 (211), Ni (111), and Pt (111). It was found that the HBE of Ni (111) was too strong, while that of $MoNi_4$ (211) was similar to Pt (111), and OH adsorption on $MoNi_4$ (211) was stronger than that of Pt (111) (Fig. 3e–g). The results can shed light on the design of other Ni-based metal alloys for the development of higher performance AEMFCs using PGM-free HOR catalysts.

3.2.3. Ni-based Heterostructures. Ideal alkaline HOR electrocatalysts are required to have delicate a balance between H_{ad} and OH_{ad} and the active sites and interaction between the components in the heterostructures.[17,61,62] Recently, many heterostructures with active interfaces have been designed with specific components for excellent HOR activity in alkaline media, such as Ni/metal oxides,[21,25,63,64] Ni/nickel carbides,[65] Ni/nickel nitrides[66,67] and Ni/nickel borides.[68] Sun *et al.* reported that the Ni/NiO active interface derived from an Ni-based MOF exhibited HOR activity with high stability and CO tolerance in alkaline media.[63] The DFT calculations demonstrated that the optimal HBE and OHBE were achieved due to the optimized equilibrium electronic and oxophilic effects at the Ni/NiO interface. Recently, Luo *et al.* reported that an oxygen vacancy-rich CeO_2/Ni hybrid exhibited efficient HOR activity in alkaline media.[25] The CeO_2-(r)/Ni sample was

Table 2 A comparison of the H_2–O_2 or H_2–air AEMFC performance of PGM-free HOR catalysts

HOR Catalysts	P_{max} (mW cm^{-2})	Current density (mA cm^{-2}/0.8 V)	Membrane	Test conditions	Ref.
Ni_3N	256 (O_2); ~150 (air)	304/0.6 V (O_2); ~140/0.6 V (air)	Alkymer®W-25	90 °C, 100% RH, 200 kPa	*Nano Lett.* 2023, **23**, 107–115.[159]
Ni–H_2–NH_3	488 (O_2); ~310 (air)	606/0.65 V (O_2); ~400/0.6 V (air)	PAP-TP-85	95 °C, 100% RH, 250 kPa	*Nat. Mater.* 2022. **21**, 804–810.[23]
Ni@C	160 (O_2)	~270/0.6 V (O_2)	QAPPT	80 °C, 200 kPa	*ACS Appl. Mater. Interfaces*, 2020, **12**, 31575–31581.[165]
NiCo/C	22 (O_2)	Not given	AT-1	60 °C, 100% RH, 130 kPa	*Energies* 2020, **13**, 582.[166]
NiCu/KB	350 (O_2)	~450/0.6 V (O_2)	Tokuyama, A201	80 °C, 100% RH, 137 kPa	*Sustain. Energy Fuels*, 2018, **2**, 2268–2275.[58]
NiMo/KB	120 (O_2)	~40/0.6 V (O_2)	Tokuyama, A201	70 °C, 70% RH, 137 kPa	*J. Mater. Chem. A*, 2017, **5**, 24433-24443.[167]
Ni–C	76 (O_2)	~120/0.6 V (O_2)	TPQPOH152	70 °C, 100% RH, 250 kPa	*Chem. Commun.* 2013, **49**, 131–133.[168]
Ni–W	40 (O_2); 27.5 (air)	~40/0.6 V (O_2); ~30/0.6 V (air)	*x*QAPS	60 °C, 100% RH, 0 kPa	*Int. J. Hydrogen Energy*, 2013, **38**, 16264–16268.[169]

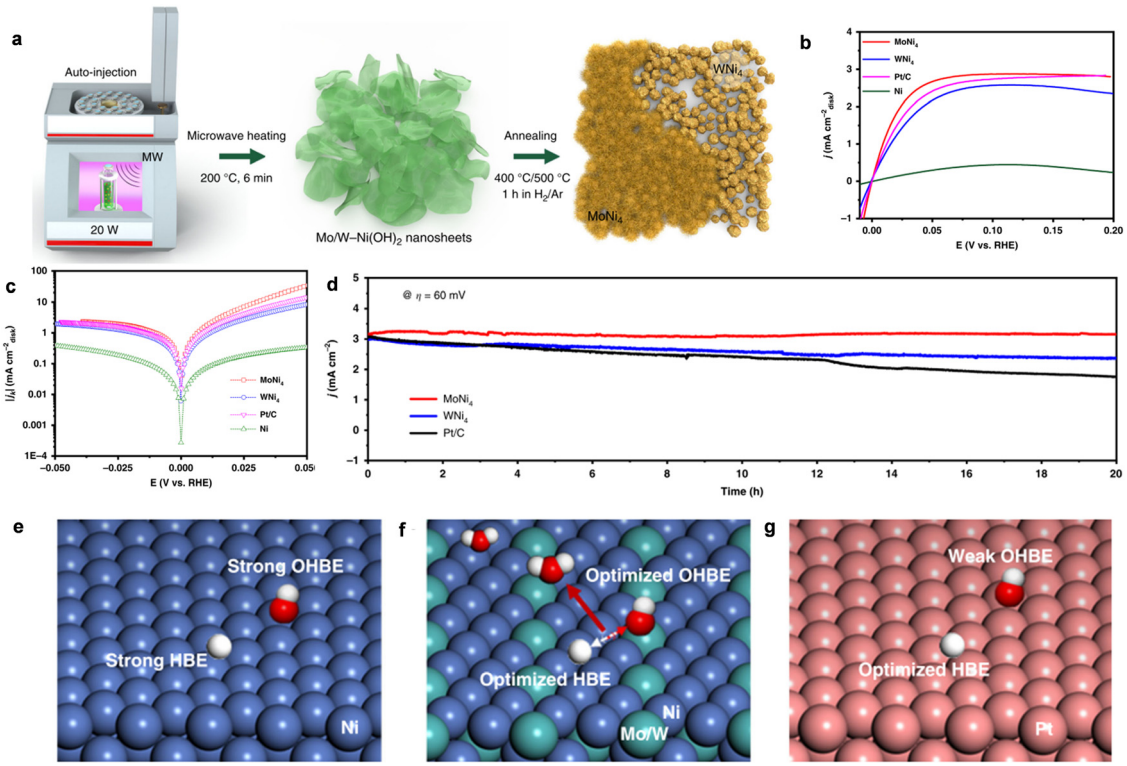

Fig. 3 (a) The synthesis of $MoNi_4$ and WNi_4 alloys. (b) The HOR polarization curves of different catalysts measured in H_2-saturated alkaline media. (c) The HOR/HER Tafel plots of the kinetic current density on $MoNi_4$, WNi_4, and reference catalysts in H_2-saturated alkaline media. (d) *i*-*t* responses recorded on $MoNi_4$, WNi_4, and Pt/C catalysts. (e)–(g) A schematic illustration of H and OH adsorption on different catalysts. Reproduced with permission from ref. 60 Copyright 2020, Nature Publications.

prepared *via* the reduction of Ni precursors in the presence of CeO_2 and XC-72. It was found that the amount of CeO_2 and oxygen vacancies in CeO_2 had a great influence on the enhanced HOR activity of Ni/C. The optimized HOR catalyst was labeled as CeO_2-(r)/Ni-1 in this work. The presence of oxygen vacancies in CeO_2 were confirmed by the of Raman spectra, as shown in Fig. 4a. The D band at 500–600 cm^{-1} was attributed to the oxygen vacancies when partial Ce^{IV} changed into Ce^{III}, while the F_{2g} band at 458 cm^{-1} represented the vibrational pattern of bulk CeO_2. The much higher intensity ratio value of the I_D/I_{F2g} bands for CeO_2-(r)/Ni-1 than that for CeO_2-/Ni-1 indicated the presence of rich oxygen vacancies in CeO_2-(r)/Ni-1. The oxygen vacancies were also confirmed from the XPS spectra, as shown in Fig. 4b. The polarization curves in Fig. 4c show the superior performance of CeO_2-(r)/Ni-1 to CeO_2/Ni-1. The exchange current density of CeO_2-(r)/Ni-1 calculated using the BV equation is depicted in Fig. 4d and its j_0 value is much higher than that of CeO_2/Ni-1. These results demonstrated the critical role of oxygen vacancies in CeO_2 in determining the high activity of CeO_2-(r)/Ni-1 for HOR. The DFT results demonstrated that the adsorption free energies of H* (ΔG_{H^*}) on pure Ni (111) was much higher than that on CeO_2-(r)/Ni (111), implying a much weaker HBE on Ni (111) after decoration with CeO_2-(r). The simulations also demonstrated the much stronger ΔG_{OH^*} than pure Ni (111), indicating that the clear active interface could significantly promote the adsorption of OH* on the surface of CeO_2-(r). The mechanism result is described in Fig. 4e, which showed that CeO_2-(r) could efficiently improve the OH* adsorption and optimize H*, well matching with the experimental enhanced HOR performance of CeO_2-(r)/Ni.

Recently, Yu and coworkers also fabricated high-activity HOR catalysts of Ni/V_2O_3 heterostructures.[21] The Ni/V_2O_3 catalyst prepared by annealing the Ni–V hydroxide nanosheet arrays on nickel foam had abundant Ni and porous V_2O_3 interfaces after the thermal treatment process. The HOR polarization curves in Fig. 4f showed that Ni/V_2O_3 catalyst delivered the lowest onset potential (~0 V), accompanying the fastest increase in anodic current compared with pure Ni and V_2O_3, demonstrating the excellent activity for HOR in alkaline media. Importantly, the HOR performance was also comparable to commercial Pt/C catalyst. Besides, the Ni/V_2O_3 heterostructures also showed great durability and higher CO tolerance than Pt/C, indicating their potential for application for AEMFCs. The DFT calculations in Fig. 4g further demonstrated that the Ni/V_2O_3 heterostructures possessed the optimal HBE and OHBE, which could greatly promote the HOR activity in alkaline media. Particularly, compared with pure Ni HOR catalysts, the Ni oxidation around the Ni/V_2O_3 interface was dramatically suppressed after long-term stability test. The O adsorption energy was further obtained, as shown in Fig. 4h, indicating that the O species were inclined to adsorb on the pure Ni catalyst with a

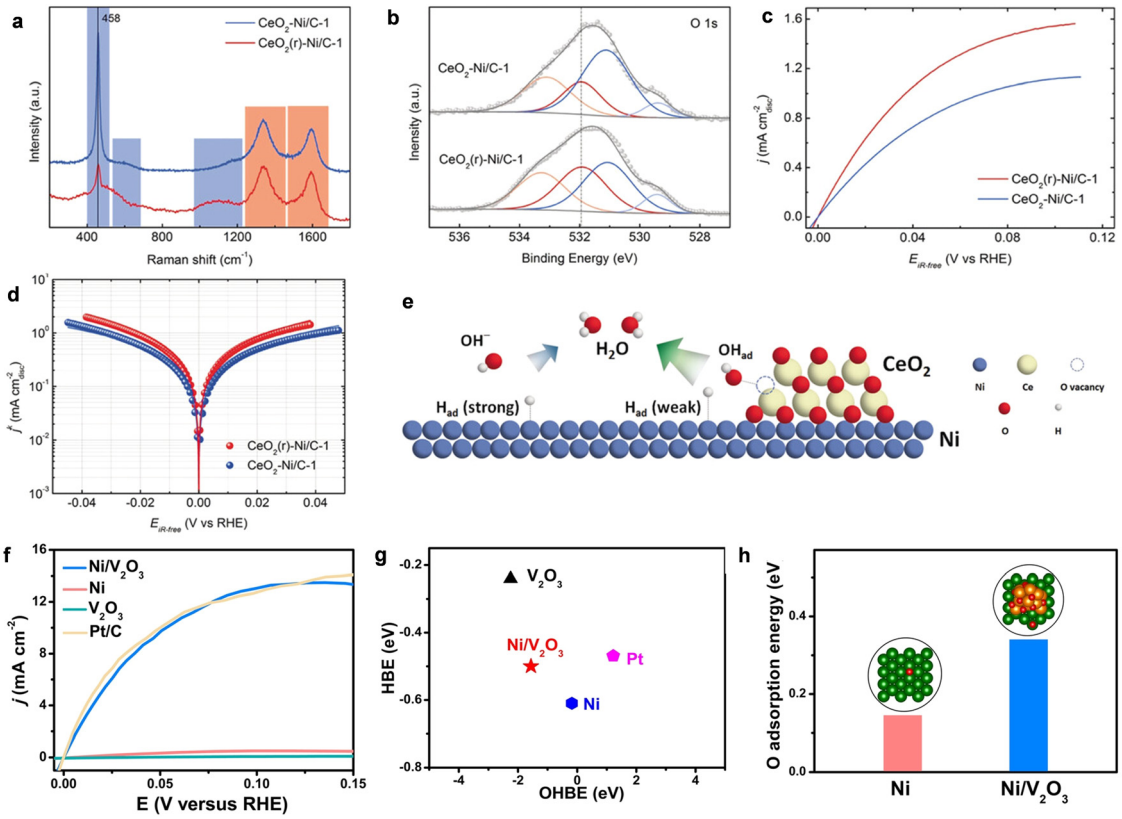

Fig. 4 (a) and (b) The Raman and XPS spectra of CeO_2 (r)-Ni/C-1 and CeO_2-Ni/C-1, respectively. (c) HOR polarization curves for CeO_2 (r)-Ni/C-1 and CeO_2-Ni/C-1. (d) The Tafel plots of CeO_2 (r)-Ni/C-1 and CeO_2-Ni/C-1. (e) A schematic illustration of the role of O-vacancy-containing CeO_2 for the HOR. Reproduced with permission from ref. 25 Copyright 2019, Wiley-VCH GmbH. (f) The HOR polarization curves for different catalysts. (g) The simulated HBE and OHBE for different catalysts. (h) The simulated O adsorption energy of Ni/V_2O_3 and Ni. Reproduced with permission from ref. 21 Copyright 2023, Wiley-VCH GmbH.

low O adsorption energy of 0.15 eV, while the O adsorption energy on the Ni/V_2O_3 heterostructures was 0.34 eV. These results imply that the Ni/V_2O_3 heterostructure was much more difficult to be oxidized than pure Ni under the alkaline HOR condition.

4. Ammonia oxidation reaction (AOR)

Compared to water electrolysis, NH_3 decomposition ($NH_3 \rightarrow N_2 + H_2$) is a more efficient way to generate H_2. For example, electrochemical water splitting requires a high voltage of 1.23 V to electrolyze the extremely stable H_2O molecules and convert them into the energy of 180 MJ to produce 1 kg H_2. However, NH_3 decomposition only requires 33 MJ of energy to produce 1 kg H_2. Thus, when NH_3 can be ideally attained in renewable ways (*e.g.*, electrosynthesis and photosynthesis), NH_3 decomposition is expected to address the future energy shortage and make the utilization of H_2 more viable.

In previous studies, the focus of NH_3 has been on hydrogen production.[69–71] However, the direct use of NH_3 as fuel is possible with the development of NH_3-fueld fuel cells (*e.g.*, DAFCs). The direct integration of AOR in fuel cells not only alleviates the demand for on-board H_2 storage, but also effectively improves the whole processes.[37,38,72] The simultaneous production of H_2 also favors the reduction of the electricity demand by incorporating fuel cells. For example, Ezzat *et al.* proposed a route that used internal combustion engines to power vehicles fueled by NH_3 and H_2 (from NH_3 decomposition). The overall energy was found to be as high as 61.89%.[73] All these possible applications can further inspire studies in AOR beyond its use for H_2 generation.

4.1. Mechanism understanding for AOR

AOR mainly follows two recognized pathways, where the first is the O–S mechanism proposed by Oswin and Salomon.[74] Specifically, NH_3 is gradually dehydrogenated to *N, and then N–N bonds bind to N_2. The second is the G–M mechanism proposed by Gerischer and Mauerer.[75] In this case, NH_3 partial dehydrogenation generates dehydrogenation intermediates $*NH_x$ (x = 1, 2), then dimerization generates hydrazine $*N_2H_x$ (x = 2, 3, 4), and finally dehydrogenation produces N_2. In both mechanisms, the reaction begins with the adsorption of ammonia and ends with the desorption of N_2. In the intermediate steps, OH^- continuously oxidizes the dehydrogenation intermediates, while the formation of $*N_2$ intermediates is the main cause of electrocatalyst poisoning. Compared with the O–S mechanism, the G–M mechanism is more widely accepted due to its lower onset potential, which has been demonstrated in many theoretical and experimental studies.[76–79] For example, Gootzen *et al.* experimentally validated

the G–M mechanism for the first time to detect the reactive *NH_x intermediates and poisoning *N adsorbents by differential electrochemical mass spectrometry (DEMS).[80] Later, Vooys *et al.* found that the adsorption strength of the metal to *N (M–N) follows the order of Ru > Rh > Pd > Ir > Pt > Au, Ag, Cu.[81] Among the single metals, Pt showed the best activity for AOR, while Au, Ag, and Cu could not combine with *NH_x or *N. The N_2H_4 intermediate was further detected by Matsui *et al.* by *in situ* attenuated total reflection infrared spectroscopy (ATR-IR) under polarization.[82] Additionally, Iglesias *et al.* recognized N_3^- by surface enhanced infrared spectroscopy (SERS) in the AOR process, which is a new reaction path involved in the G–M mechanism.[78] Additionally, Skachkov *et al.* found that two mechanisms can compete depending on the reaction potential.[76] The O–S mechanism was dominant at a moderate reaction potential (+0.5 V *vs.* RHE), while the G–M mechanism governed at a lower surface potential (<0.5 V *vs.* RHE).

Later, Herron *et al.* studied the catalytic AOR on different metals with close-packed surfaces by first-principles study.[83] They estimated the onset potentials of different metals, following the order of Co < Pd < Pt < Ir < Ni < Cu based on the G–M mechanism, as shown in Fig. 5a. Although Co showed the lowest onset potential, the simulated high N–N bond formation barriers severely limit the activity of Co for AOR. Based on the Sabatier analysis, the surface activity at 0 V against N–N binding formation barriers followed the order of Pt > Ir > Cu > Pd > Rh > Co, implying that Pt has the highest activity, followed by Ir (Fig. 5b). Based on the volcano plot found in this study, precious metals such as Pt, Pd and Ir are limited by their strong M-N bonds. In contrast, metals such as Au, Ag and Cu binds to N weakly; however, they are inactive for N_2 formation. Among the studied metals, Cu shows theoretically high AOR activity; however, a high overpotential of 1.22 V is required to lower the barrier of the electrochemical step due to the too weak Cu–N bond. Thus, it was concluded that Pt shows the best AOR activity followed by Ir and Cu and the optimal catalyst should process an M–N bond energy that is between Pt–N and Cu–N. Notably, the presence of the N–N coupling step and the strong *N adsorbent can result in the severe poisoning of the active surface. Besides the strong adsorbent of *N that can poison the active surface, Matsui *et al.* found that the generation of oxygenated nitrides could also determine the whole AOR, as well as the tight interaction between *NO_x species and Pt surface could significant hinder the formation of N_2.[82] Compared with direct H_2/methanol fuel cells, DAFCs remain at a low technical level due to the more complicated and sluggish kinetic of AOR than the competing *H adsorption.[2] Consequently, in the design of catalysts for AOR with high efficiency, it is necessary to simultaneously suppress the H adsorption at the anode side of DAFCs.

4.2. Recent electrocatalysts for AOR

4.2.1. Molecular electrocatalysts. Currently, there are three main types of electrocatalysts for AOR, including molecular catalysts, Pt-based precious metals and non-precious metal-related catalysts. The development of AOR by molecular electrocatalysts is rapid but still in its infancy.[84–86] A recent review discussed the promising opportunities and gave new perspectives on the design of molecular catalysts with efficient activity for AOR.[87] Particularly, three critical parameters have been illustrated to design efficient molecular catalysts, namely, low N–H bond energy, favorable N_2 production dissociation and exergonic N–N coupling. In general, group IV–VI materials endowed with electron-rich characteristics show relatively low N–H bond energies, probably due to their strong ability to produce multiple metal–ligand bonds and tendency to form high oxidation states. Unlike the previously known Ru-based noble molecular electrocatalysts, Zott *et al.* reported the preparation of first-row iron(II) tris(2-pyridylmethyl)amine (TPA) bis-ammine triflate AOR electrocatalysts,[84] as shown in Fig. 6a. Cyclic voltammetry experiments indicated that in the presence of NH_3, the onset potential was obvious under the condition of 0.7 V *vs.* Fc/Fc^+, and the attenuation of catalytic current was negligible after 50 continuous cyclic voltammetry (CV) cycles, indicating the robust stability of TPA-connected Fe to AOR (Fig. 6b). In contrast, there was a continuous decrease in the peak current using $FeOTf_2$ as the anode catalyst, which was attributed to the instability of $[Fe(NH_3)_6]OTf_2$ (formed by $FeOTf_2$ existing in the presence of NH_3) under the catalytic conditions. The formation of the Fe^{III}–NH_2 intermediate (at 0.4 V) in the electrochemical studies

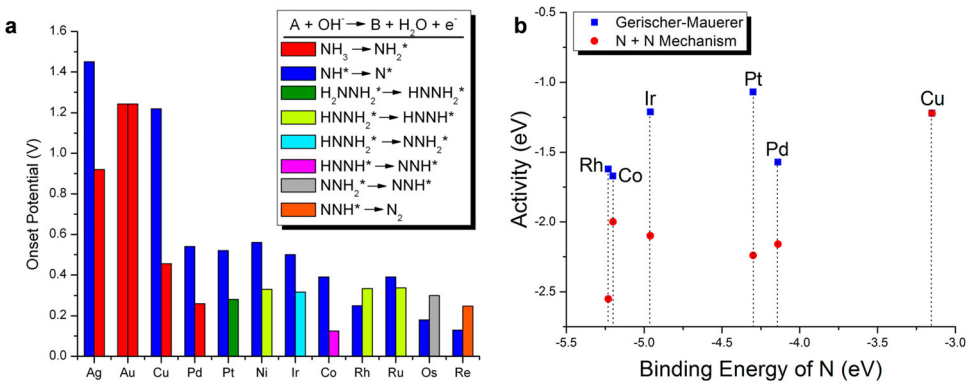

Fig. 5 (a) Onset potential investigation for different transition metals. (b) The AOR activity predicted by both mechanisms. Reproduced with permission from ref. 83 Copyright 2015, ACS publications.

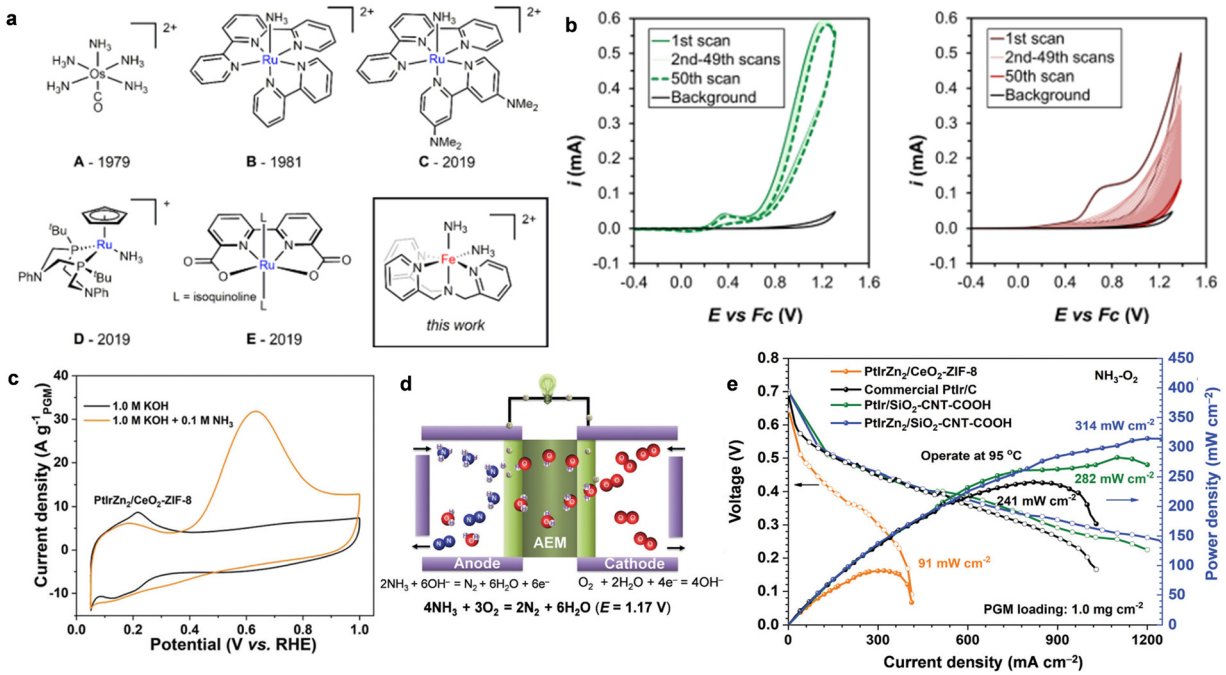

Fig. 6 (a) Representative molecular complexes that catalyze the AOR. (b) The cycling of 2.5 mM $[(TPA)Fe(MeCN)_2]OTf_2$ (left) or 2.5 mM $FeOTf_2$ (right) in CH_3CN+ 50 mM NH_3 or CH_3CN + 50 mM NH_4OTf solution. Reproduced with permission from ref. 84 Copyright 2019, ACS publications. (c) CV curves of the AOR activity of $PtIrZn_2/CeO_2$-ZIF-8 in the presence and absence of NH_3. (d) A schematic view of the DAFC single cell. (e) The polarization curves and power density curves of DAFCs with different anode catalysts. Reproduced with permission from ref. 38 Copyright 2020, The Royal Society of Chemistry.

indicated that N–N bond formation facilitates the reaction process. Based on the above-mentioned strategies, molecular electrocatalysts for AOR show great prospects.

4.2.2. PGM-related electrocatalysts. In heterogeneous electrocatalysts, Pt is the most active metal electrocatalyst for AOR to N_2, accompanied by an overpotential of >0.4 V on the surface of polycrystalline Pt.[34,88] It was demonstrated that a single-crystal Pt electrode, the (100)-type surface was the dominant active site.[89] Additionally, the Pt surface is deactivated by the strong adsorbing reaction intermediate, such as N_{ad} and NO_{ad} at above 0.6 V, indicating that a higher overpotential can drive a higher AOR rate. Alloying Pt with Ir can effectively lower the onset potential towards N_2 with an increase in temperature (>80 °C),[2] in which the formation of *N intermediates can occur at a relatively low overpotential with a high reaction rate for a kinetically favorable AOR.[90] However, Ir is more expensive and scarce than other Pt group metals, and hence exploring Pt-based alloys with earth-abundant elements can be a viable way to minimize the utilization of Ir and enhance the AOR activity and durability. For instance, Wu *et al.* reported the preparation of ternary PtIrZn alloys ($\sim$2 nm in particle size) that were highly dispersed on binary CeO_2 and ZIF-8-derived N-doped carbon substrates ($PtIrZn/CeO_2$-ZIF-8),[38] as shown in Fig. 6c. The as-fabricated catalysts showed high AOR activity with an onset potential of 0.35 V, which is lower than that of PtIr/C (0.43 V) in alkaline media. The DFT calculations suggested that doping of Zn in PtIr alloys can facilitate the stronger $*NH_3$ adsorption than *H adsorption, thereby kinetically triggering AOR with high performance. When $PtIrZn/CeO_2$-ZIF-8 was used as the anodic catalyst in an AEM-DAFC (Fig. 6d and e), the peak power density was 91 mW cm^{-2}. Additionally, when PtIrZn alloys were fabricated on binary substrates composed of SiO_2 with a large surface and conductive CNT-COOH ($PtIrZn/SiO_2$-CNT-COOH), the anode catalyst reached a remarkable peak power density of 314 mW cm^{-2} as a result of the decreased charge transfer resistance and increased mass transport. Thus, the successful alloying strategies show great promise for the exploration of more Pt-based ternary, quaternary alloys with enhanced catalytic activity for AOR.

4.2.3. Non-precious metal-related electrocatalysts. The possibility of using noble-metal free electrocatalysts in an alkaline operating environment is one of their most important advantages. PGM-related AOR catalysts are the most widely studied and intensively reviewed.[91,92] However, the utilization of PGM-related catalysts is limited due to their high-cost, scarcity and instability. Recently, Ni-related PGM-free catalysts have been demonstrated as promising alternatives to PGMs given that they are more affordable and have higher intrinsic AOR activity. For example, Ni is predicted to exhibit a low onset potential of 0.33 V *vs.* RHE for AOR. However, the strong Ni-N bonding leads to a high energy barrier of 1.39 eV for the formation of hydrazine species.[83] Generally, pure Ni metal delivers poor activity for AOR; however, the activated species such as $Ni(OH)_2$ layer and NiOOH were demonstrated to be responsible for AOR.[93,94] Presently, Ni-based catalysts are often restrained by their easy corrosion, which can severely degrade the overall efficiency. Thus, to overcome this limitation, alloying Ni with metals possessing high AOR activity but low affinity

for N is a promising pathway. In this case, Cu is a typical metal with a low Cu–N binding strength, which can effectively enhance the AOR activity due to the increment in active sites.[95,96] For instance, Xu *et al.* reported the synthesis of NiCu layered hydroxide (LH) nanowires grown directly on carbon cloth *via* the hydrothermal method.[96] As shown in Fig. 7a, both $Ni(OH)_2$ and $Ni_{0.8}Cu_{0.2}$ LHs showed approximate onset potentials, which were mainly caused by the generation of NiOOH and $Ni_{0.8}Cu_{0.2}OOH$, respectively. Interestingly, the current density of the $Ni_{0.8}Cu_{0.2}$ LHs increased sharply in potential regions above the onset potential, manifesting their higher AOR activity than $Ni(OH)_2$. Moreover, the chronoamperometry tests, as shown in Fig. 7b, demonstrated that the current density of $Ni_{0.8}Cu_{0.2}$ LHs increased to ~35 mA cm^{-2} by a factor of 6 times, further confirming the significant enhancement in AOR activity by Cu doping. It was also demonstrated that the concentration of NH_3 had a great effect on the AOR activity of $Ni_{0.8}Cu_{0.2}$ LHs, as shown in Fig. 7c. The AOR current was found to gradually increase upon the step-wise injection of NH_3, demonstrating that the $Ni_{0.8}Cu_{0.2}$ LHs still showed activity at high NH_3 concentrations. Intriguingly, the increase in current was slowed down when the NH_3 concentration was higher than 130 mM, which was probably caused by the saturation of the active sites on the surface of $Ni_{0.8}Cu_{0.2}$ LHs. In this work, the choice of doping elements was further studied. The AOR activity of five bimetal NiM LHs (M = Co, Fe, Zn, Mn, Cr) was compared but negligible AOR activity was detected for all five catalysts.

MAFCs have been widely studied to remove NH_3 in wastewater, as noted above. However, the main performance parameters of an MAFC, such as maximum power density and NH_3 removal efficiency, are random in practical applications because of the deterioration of the catalyst and biofouling. Hence, Tao *et al.* reported the fabrication of an AEM-DAFC, integrating an α-MnO_2/C cathode and NiCu/C anode for the treatment of NH_3-rich wastewater.[97] The schematic process is shown in Fig. 7d. Additionally, the leachate was collected to evaluate the application of the AEM-DAFC. It was expected that NH_3 can be effectively removed from the leachate as well as electricity is produced from the fuel cell as a bonus. As expected, the open circuit voltage (OCV) increased with an increase in the NH_3 concentration (Fig. 7e). The maximum power density was as high as 0.35 mW cm^{-2} when the NH_3 concentration was 3 M (Fig. 7f). Moreover, a power density of 0.11 mW cm^{-2} was obtained for real wastewater containing ~0.12 M NH_3, indicating its very promising application.

5. Oxygen reduction reaction (ORR)

5.1. Mechanism understanding for ORR

ORR involves two reaction pathways in alkaline media, *i.e.*, $2e^-$ (HO_2^-) and $4e^-$ (OH^-) reduction, and their adsorption mode, activation and cleavage barrier on the surface of the catalyst comprehensively determine the activity.[98,99] Between them, $2e^-$ reduction is not thermodynamically favorable for fuel cells, and some reviews have made insightful summaries for this important reaction,[100–102] and thus it will not be introduced in this review. Generally, the $4e^-$ ORR process in the alkaline media is as follows:

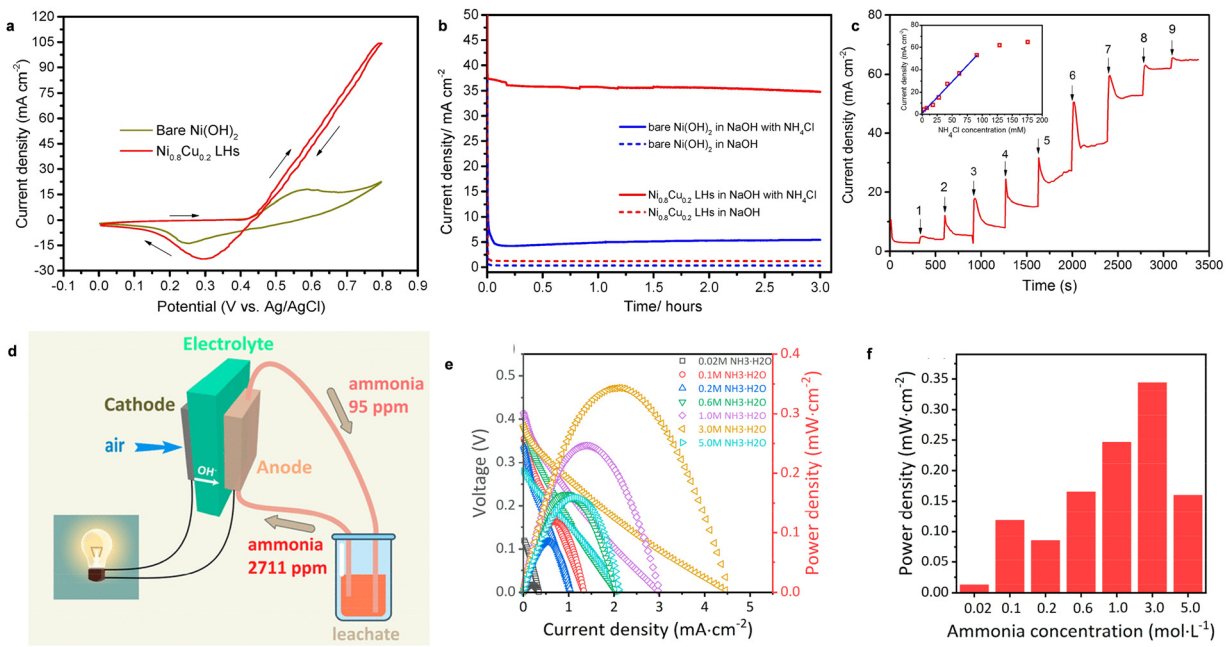

Fig. 7 (a) CV of $Ni_{0.8}Cu_{0.2}$ LHs and bare $Ni(OH)_2$ in NH_3-containing electrolyte. (b) The chronoamperometry curves of $Ni_{0.8}Cu_{0.2}$ LHs and bare $Ni(OH)_2$ with and without NH_3. (c) The current response of $Ni_{0.8}Cu_{0.2}$ LHs to injection of NH_4Cl solution. Reproduced with permission from ref. 96 Copyright 2017, Elsevier. (d) A schematic process of the AEM-DAFC device. (e) The *I*–*V* curves and (f) power density of an AEM-DAFC at different ammonia concentrations using the MnO_2/C cathode and NiCu/C anode at room temperature. Reproduced with permission from ref. 97 Copyright 2020, ACS Publications.

$$O_2 + 2H_2O + 4e^- = 4OH^-;\ E^0 = 1.23\ V\ vs.\ RHE$$

$$O_{2\ (g)} + * \rightarrow O^*_2 \quad (5.1)$$

$$O_2 + * + H_2O + e^- \rightarrow OOH^* + OH^- \quad (5.2)$$

$$OOH^* + e^- \rightarrow O^* + OH^- \quad (5.3)$$

$$O^* + H_2O + e^- \rightarrow OH^* + OH^- \quad (5.4)$$

$$OH^* + e^- \rightarrow OH^- + * \quad (5.5)$$

In the ORR process, O_2 initially fills the electrolyte, and then adsorbed on the surface of the electrocatalyst. Subsequently, the O–O bond is dissociated from the hydrogenation of the O_2 intermediate, which can determine the $4e^-$ or $2e^-$ ORR pathway. Finally, the OH^- ions on the surface of the catalyst are further released into the alkaline medium. During the $4e^-$ ORR process, multiple oxygen intermediates including O*, OH* and OOH* are involved in the adsorption and desorption processes. In contrast, only OOH* occurs as the intermediate in the $2e^-$ ORR process. Activation of the O–O bonds can be achieved by binding to the catalytic sites. The electronic environment around the active site also varies the electron distribution of O–O, and thus influences the activation. O–O can be adsorbed sideways on the active site or end-adsorbed on a single active site, thereby weakening the O–O bond, facilitating the dissociation process.[98,103] However, the strong interaction between the active site and O_2 for many catalysts impedes the removal of H_2O_2 formed during dissociation and binding, thus preventing the further reduction of *OOH to H_2O.[103] In end-on adsorption, $2e^-$ reduction is advantageous if the binding strength is not sufficient to dissociate O_2 and leads to the final generation of H_2O_2, which has been detected in many carbon-related materials.[99]

In ideal catalysts, the binding of different oxygen intermediates is required. In less surface-active catalysts, the O_2 adsorption step is generally regarded as the rate-limiting step (RLS) in comparison with the adsorption of the ORR intermediates (OOH*, O*, and *OH). However, Nørskov *et al.* considered that the adsorption of O_2 is a chemical step rather than the RLS, assuming a simple electron–proton transfer process involved for simplification.[98] The free energy of the intermediate products can be used as a basis for understanding the ORR mechanism and the potential barrier is mainly determined by the free energy of the intermediates according to the simulation results. The ΔG of the reaction intermediate can be expressed according to the computational hydrogen electrode (CHE) model as follows:

$$\Delta G = \Delta E_{elc} + \Delta E_w + \Delta E_{field} + \Delta ZPE - T\Delta S - neU \quad (5.6)$$

where ΔE_{elc} represents the simulated binding (adsorption) energy, ΔE_W and ΔE_{field} represent the effects of adsorbate solvation and electric field, ΔZPE and $T\Delta S$ represent the zero-point energy and entropic corrections, respectively, and eU is the free energy of a single H^+/e^- pair.

The equilibrium potential in a $4e^-$ ORR process is 1.23 V (Fig. 8a), and $O_2 \rightarrow$*OOH and *OH $\rightarrow H_2O$ must conquer a free energy barrier. On Pt (111), when both reactions are exergonic (such as a high ORR current occurs), the calculated maximum potential (thermodynamic limit potential, U_L) is about 0.8 V for Pt (111). One benchmark for ORR performance is the theoretical potential (η_{theo}) calculated by subtracting the U_L from the equilibrium potential, where η_{theo} = 1.23 V–0.8 V = 0.43 V for Pt (111). Additionally, the CHE-based theory was also intensively used to demonstrate the trends in ORR performance for various types of materials, for example, transition metals,[104] oxides,[105–107] sulfides[108] and carbon-related materials.[109,110] For more details about the ORR mechanism on different types of catalysts, the previous reviews can be referenced.[111]

As shown in Fig. 8b, the binding energies of intermediates for different metals are closely related and monotonically vary. The linear relationships arise from the sorbents binding to the surface through an O atom. Particularly, the slope of the *OOH → *OH line is ~1, implying that the two adsorbents possess similar metal–oxygen single bonds. Differently, the slope of the scale lines of *O → *OH is ~2, and the adsorbed O forms a double bond with the surface, while *OH is combined by a single bond.[112] The *OOH-related scaling relationship to *OH or *O means that one independent variable can describe the binding free energy of the intermediates under preliminary approximation. Recently, the *O associative free energy (ΔG_O) and the *OH associative free energy (ΔG_{OH}) have

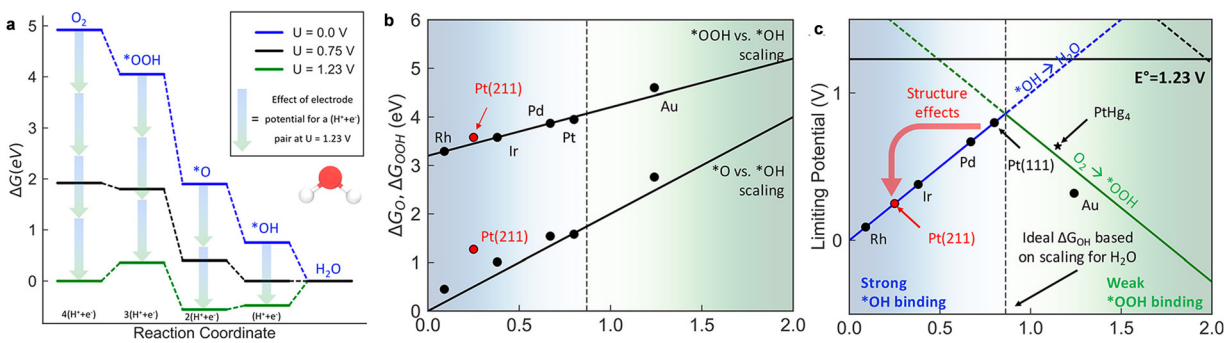

Fig. 8 (a) The free energy diagram for the $4e^-$ associative ORR on Pt (111); (b) scaling relationships for the chemisorption energies of *OOH and *O against *OH for the (111) surface of different metals [$\Delta G_{(*OOH)} = \Delta G_{(*OH)} + 3.2$; $\Delta G_{(*O)} = 2\Delta G_{(*OH)}$]; and (c) limiting potentials for individual steps in Equations 5.7–5.10, exhibiting the strongly bound *OH region (solid blue line) and weakly bound *OOH region (solid green line) for the $4e^-$ process. Reproduced with permission from ref. 98 Copyright 2018, ACS Publications.

been widely reported due to the good scaling between *OOH and *OH, as shown in Fig. 8b.[113] The U_L as a function of the adsorption of OH free energy can be defined as follows:

$$U_{L1} = -\Delta G_{OH} + 1.72 \quad (5.7)$$

$$U_{L2} = -\Delta G_{OH} + 3.3 \quad (5.8)$$

$$U_{L3} = -\Delta G_{OH} \quad (5.9)$$

$$U_{L4} = -\Delta G_{OH} \quad (5.10)$$

According to the above-mentioned equations, the $U_{L1–L4}$ lines of the four basic steps in Fig. 8c are obtained. The lowest limit potential of the catalytic reaction determines the limit potential of the entire reaction, as represented by solid blue and green lines. For metals with strong binding *OH, *OH → H_2O is the potential limit, while the activation of O_2 → *OOH is the potential limit for weak binding metals. Undoubtedly, Pt is located at the top of the limit potential volcano.[114] Moreover, the analysis has been used to explain the structural sensitivity of ORR. Given that other dense transition metal sections are roughly arranged along the (111) *OOH *vs.* *OH scale lines, they are described by the one-dimensional volcanoes in Fig. 8c. The *OH bond on the (211) face on the terrace is stronger (more negative ΔG_{OH}) than on the (111) terrace. For example, although Pt (111) exhibits an excellent ORR performance, strong binding at (211) leads to surface adsorbed *OH poisoning (Fig. 8c). This explains the reduced performance of Pt particles with a smaller size, given that smaller particle sizes can result in more devitalized step sites.[115] Alternatively, the step can increase activity and may require smaller particle sizes for catalysts on the weakly bound side.[116]

5.2. Electrocatalysts for ORR

AEMFCs show many advantages compared to PEMFCs, for example, wider choices for bipolar plates and more enhanced ORR kinetics in alkaline media than in acid media. Particularly, due to their enhanced kinetics, it is expected that PGM-free catalysts can be utilized. Hence, in this part, PGM-based catalysts will not be introduced. Table 3 presents a comparison

Table 3 A comparison of H_2–O_2 or H_2–air AEMFC performance of PGM-free ORR catalysts

ORR catalysts	P_{max} (mW cm^{-2})	Current density (mA cm^{-2})	Membrane	Test conditions	Ref.
ZnNC	503 (air)	140 (air)	PAP-TP-85	80 °C, 100% RH, 150 kPa	*Angew. Chem., Int. Ed.* 2023, **62**, e202216041.[125]
FeCo-NCH	569 (O_2); 299.3 (air)	~85/0.9 V (O_2); < 150/0.8 V (air)	PAP-TP-85	80 °C, 200 kPa, 100% RH	*Nat. Commun.* 2023, **14**, 1822.[170]
NDPC-1000	913 (O_2); 597 (air)	261/0.8 V (O_2); ~125/0.8 V (air)	PAP-TP-85	80 °C, 2.5 kPa	*Adv. Energy Mater.* 2023, **13**, 2204390.[171]
FeCu–NC	1090 (O_2); 660 (air)	574/0.8 V (O_2); 282 (air)	Alkymer W-25	80 °C, 150 kPa, 100% RH	*Adv. Energy Mater.* 2023, 2302719.[172]
Ni_3N||ZrN	151 (air)	~50 (air)	Alkymer®W-25	90 °C, 200 kPa	*Nano Lett.* 2023, **23**, 107.[159]
HT-FeCu porphyrrole	510 (O_2);	~85/0.8 V (O_2)	Versogen, PiperION-A-20HCO_3	80 °C	*ACS Catal.* 2023, **13**, 11012.[173]
$Co_{NP}/CNH_{8.1\%}$ NH_3	619 (O_2)	880/0.6 V (O_2)	FAA-3-50	60 °C	*Appl. Catal. B Environ.* 2023, **323**, 122172.[174]
$MnCo_2O_4$	310 (air)	~120 (air)	PAP-TP-85	95 °C, 250 kPa	*Nat. Mater.* 2022, **21**, 804.[23]
o-MQFe10 : 20:5	407.5 (O_2)	290/0.6 V (O_2)	Tokuyama A201	80 °C, 150 kPa, 100% RH	*Angew. Chem., Int. Ed.* 2022, **61**, e202117617.[175]
Cu–N–C/GC	324 (O_2)	~75/0.8 V (O_2)	aQAPS-S 8	60 °C, 200kPa, 100% RH	*Angew. Chem., Int. Ed.* 2022, **61**, e202211098.[176]
Co_3N/C	700 (O_2)	~125/0.8 V (O_2)	QAPPT	80 °C, 200kPa, 100% R	*Sci. Adv.* 2022, **8**, 1584.[177]
FPD-Co	654 (O_2); 323 (air)	760/0.6 V (O_2); ~40/0.8 V (air)	PTFE	80 °C, 100% RH, 200 kPa	*Proc. Natl. Acad. Sci. U. S. A.*2022, **119**, e2214089119.[178]
FeCoNCMgOAc	920 (O_2)	200/0.8 V (O_2)	Radiation-grafted LDPE	55 °C	*ACS Catal.* 2022, **12**, 14050.[179]
Fe–Mn–N–C	1320 (O_2); 605 (air)	1200/0.65 V (O_2);	PAP-TP-85	80 °C, 100% RH, 250 kPa	*Appl. Catal. B Environ.* 2022, **317**, 121770.[180]
Ag_{NPs}@Fe–N–C	848 (O_2); 404 (air)	~250/0.8 V (O_2); < 125/0.8 V (air)	PAP-TP-85	80 °C, 100% RH, 200 kPa	*Nano Energy* 2022, **100**, 107466.[124]
CoTPyP@ImRGO	528 (O_2)	461/0.6 V (O_2)	alkaline polymer membrane	80 °C, 200 kPa	*Nano Energy* 2022, **101**, 107565.[181]
O-FeN_4C-O	540 (air)	~125 (air)	PAP-TP-85	80 °C, 100% RH, 200 kPa	*Chem Catal.* 2022, **2**, 2750.[182]
Fe–N–C	2050 (O_2); 1010 (air)	920/0.8 V (O_2); 130/0.8 V (air)	HDPE	80 °C, 100% RH, 200 kPa	*Nat. Energy* 2021, **6**, 834.[123]
PF-TMPPCo	226 (O_2)	250/0.6 V (O_2)	HDPE-25 μm	60 °C, 0 kPa, 75% RH	*Angew. Chem., Int. Ed.* 2021, **60**, 4049.[134]
Fe^{2+}@NCS-A	~108 (O_2)	~12.5/0.8 V (O_2)	Radiation-grafted LDPE	60 °C, 0 kPa, 100% RH	*Adv. Funct. Mater.* 2021, **31**, 2102974.[183]
HT800-FeP	580 (O_2)	125/0.8 V (O_2)	ETFE-BTMA	80 °C, 100 kPa	*Adv. Funct. Mater.* 2021, **31**, 2100963.[184]
Fe–N–C	1440 (O_2)	~250/0.8 V (O_2)	Not given	65 °C	*ACS Catal.* 2020, **10**, 225–234.[185]
N–C–CoOx	1050 (O_2); 660 (air)	290/0.8 V (O_2);80/0.8 V (air)	LDPE-BTMA	65 °C, 100% RH, 80 kPa	*Angew. Chem., Int. Ed.* 2019, **58**, 1046-1051.[186]

of the performance of H_2–O_2 or H_2–air AEMFCs consisting of PGM-free ORR catalysts.

5.2.1. Pyrolyzed carbon-based ORR catalysts. Since Jasinsky *et al.* found that the macrocyclic compound phthalocyanine cobalt had good ORR activity in 1964,[117] intense studies on the replacement of PGM catalysts by transition metal (TM) materials as ORR catalysts have been carried out. Nevertheless, the high cost of macrocyclic compounds hinders their extensive utilization. In 1989, Yeager *et al.* proposed a model in which electronically conductive surfaces with N-groups can couple with TM metals to form TM–N_x structures by finely selecting appropriate TM, N, and carbon precursors.[118] This model offers an effective and economical way to fabricate catalysts by thermal treatment of iron salts and N- and C-containing precursors. At present, the ORR activity of M–N–C catalysts is close to or even outperforms PGMs in alkaline media.

M–N–C catalysts, as the most viable alternatives to PGMs, have attracted significant attention because of their low cost and high intrinsic ORR activity. In particular, many researchers are committed to exploring low-cost and efficient ORR catalysts with the fast development of atomically dispersed catalysts (ADCs). Generally, the state-of-the-art Fe–N–C catalysts have delivered $E_{1/2}$ potentials as high as 0.85 V in alkaline media, which are comparable to commercial Pt/C.[7,119,120] Various strategies of synthesizing M–N–C-based ADCs and their application in PEMFCs or zinc–air batteries have been reviewed.[11,121,122] However, when Fe–N–C ORR catalysts are integrated in the AEMFCs, they show a poor performance compared with Pt/C cathodes because of the inefficient mass transport and low catalyst loading. Thus, to address this problem, Mustain *et al.* developed the utilization of a commercial Fe–N–C catalyst with single-atom Fe–N_x sites in the AEMFC cathode.[123] The Fe–N–C catalysts were further modified by increasing their average pore size to facilitate the efficient transport of generated H_2O on the anode side in the CLs, as well as increasing the graphitization of the catalyst to decrease the hydrophilicity (Fig. 9a). The average pore size was increased by mixing amorphous fumed SiO_2 with Fe metal salt and NC precursors, followed by high-temperature pyrolysis. Upon removing the SiO_2 template, the final desired Fe–N–C catalyst was obtained by a second pyrolysis to increase the degree of graphitization. The as-prepared Fe–N–C catalyst showed a high $E_{1/2}$ of 0.846 V, which is comparable to Pt/C at different rotating rates in the rate of 400–2500 r.p.m (Fig. 9b). Additionally, it was found that water management played important roles to guarantee the high-performance and durability, as shown in Fig. 9c. When the cell was operated under high water accumulation at the anode (anode/cathode/cell temperature: 60/60/60 °C) with full humidity, the cell performance was low. Once the cell temperature was evaluated at 70 °C, the peak powder density correspondingly increased. Additionally, applying backpressure to the cathode could also significantly increase the cell performance, while it shows the opposite effect for the anode side, as shown in Fig. 9c (blue curve).

Although Fe–N–C shows higher ORR activity than commercial Pt/C in alkaline media, Fe–N–C catalysts often suffer from the unsatisfactory stability because the Fe^{2+} intermediates tend to generate the Fenton effect, which impairs the active sites and the polymer membrane. To enhance the stability of Fe–N–C for ORR, Cao *et al.* developed an Ag_{NP}@Fe–N–C composite catalyst, showing an efficient ORR performance and robust stability.[124] After assembling an AFMFC, the catalyst showed extremely high peak power density (0.848 W cm^{-2}) and long-term device durability of 200 h in an H_2/air (CO_2-free) system. Later, they reported the synthesis of a ZnNC catalyst, which showed

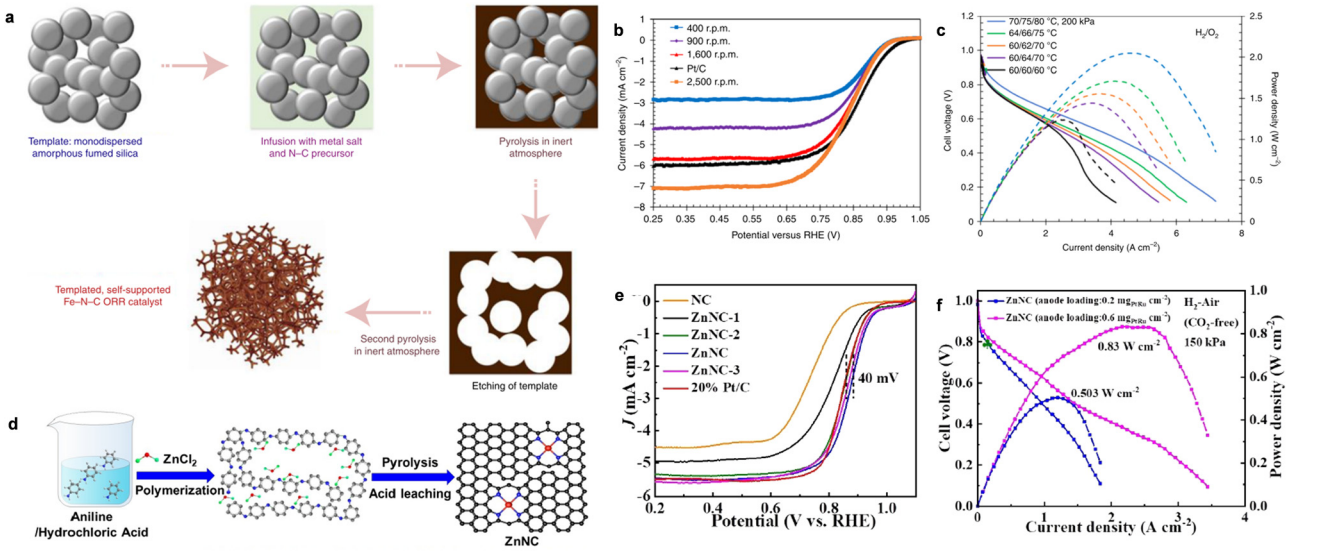

Fig. 9 (a) The synthesis of the desired structure of the Fe–N–C catalyst. (b) The ORR LSV curves of Fe–N–C at different rotating rates compared to Pt/C. (c) The H_2–O_2 AEM performance of the Fe–N–C cathode. The curves were obtained with 1 mg cm^{-2} Fe–N–C as the cathode and 0.6 mg cm^{-2} PtRu as the anode. Reproduced with permission from ref. 123 Copyright 2021, Nature Publications. (d) The synthesis of ZnNC. (e) The LSV curves of ZnNC with different reference catalysts. (f) The polarization and power density curves of H_2–air (CO_2-free) AEMFC with ZnNC in the cathode and PtRu/C in the anode. Reproduced with permission from ref. 125 Copyright 2022, Wiley-VCH GmbH Publications.

efficient ORR activity with long-time stability and Fenton reaction-inactivity.[125] The ZnNC catalyst was prepared by calcining a mixture of Zn-doped polyaniline and NH_4Cl at 900 °C in an Ar atmosphere, as shown in Fig. 9d. The final ZnNC was obtained with special Zn-pyrrolic structures and showed superior ORR performance to commercial Pt/C (Fig. 9e). Also, the assembled H_2–O_2 AEMFC under the Department of Energy (DOE) testing protocol showed a peak power density of 1.17 W cm^{-2}. Importantly, the current density was as high as 1.17 A cm^{-2} at 0.65 V, surpassing the DOE 2022 target of 1.0 A cm^{-2} at 0.65 V (Fig. 9f). The peak power density performance for ZnNC could also reach 0.83 and 0.50 W cm^{-2} when varying the anode loading to 0.6 mg_{PtRu} cm^{-2} and 0.2 mg_{PtRu} cm^{-2}, respectively, in the H_2–air (CO_2-free) system (Fig. 9g). The breakthrough of the highly durable ZnNC ORR catalyst paves the way for the preparation of cheap and durable AEMFCs.

5.2.2. Pyrolysis-free ORR catalysts. Transition-metal complexes of N-containing ligand- and macrocycle-based molecular catalysts, including metallo-porphyrins (Py), corroles, and phthalocyanines (Pc), have been attracting intensive attention as promising alternatives to Pt-related ORR catalysts since the discovery of CoPc for catalysis of ORR in 1964.[99,117,126–131] Nevertheless, most molecular catalysts for homogeneous catalysis are not as active as their pyrolyzed analogues for heterogeneous catalysis, particularly in acid media. Recently, the advances in AEMFC have increased the interest in molecular catalysts, which have been demonstrated to have high activity and stability in alkaline media.[132,133] Importantly, molecular catalysts can exist in the same electrolyte as the reaction substance during the homogeneous catalysis process. Therefore, a very high utilization rate of the molecular catalyst can be obtained; moreover, the slow mass transfer problem occurring in heterogeneous catalysts can be avoided. In general, molecular catalysts are mixed with carbon supports or directly deposited on the surface of diffusion electrodes; however, there are still challenges that need to be addressed. For example, the low electronic conductivity, random distribution and stability of molecular catalysts upon the simultaneous reactions of O_2, ions and electrons in homogenous catalysis.

Thus, to solve these problems, He *et al.* designed a homogeneous composite catalyst by combining 5,10,15,20-[tetrakis-(4methoxyphenyl)porphyrin]cobalt(II) (TMPPCo) with a high-performance anion exchange ionomer of polyfluorene (PF).[134] In the PF-TMPPCo composite catalyst layer, as shown in Fig. 10a, the TMPPCo molecular catalyst was evenly immobilized on the size chain of the ionic conductive polymer, which could favor the microphase separation process and high density distribution of active sites. Benefiting from the covalent immobilization strategy, PF-TMPPCo showed a superior ORR performance to the reference catalysts, as shown in Fig. 10b. The $E_{1/2}$ of PF-TMPPCo was as high as 0.81 V, showing a 40 mV higher value than that of PFI-TMPPCo (physical mixture of PF ionomer and TMPPCo), confirming that the homogeneous composite catalyst could enable the molecular catalysis process in the three-phase interface. Additionally, PF-TMPPCo showed a superior AEMFC performance with the peak power density of 226 mW cm^{-2} (Fig. 10c), which was much better than that of PFI-TMPPCo (58 mW cm^{-2}). The reshaped catalyst layer design could significantly improve the mass transfer of O_2, H_2O and H_2O_2, as well as the utilization of the Co active sites in the homogeneous catalytic process.

It is well known that metal–organic frameworks (MOFs) are one of the most important porous inorganic–organic hybrid materials, which have attracted much scientific interest in the field of energy conversion.[135,136] Benefiting from their high specific surface area, tunable porous sizes and high accessibility of the active sites, MOFs can act as catalytic centers or porous supports during heterogeneous catalysis. One of the important advantages of MOFs is their flexible design and tunable porous size and functionality at the molecular level. It has been demonstrated that metalloporphyrin molecules show strong interactions with O_2 and provide a great opportunity as channels for fast electron transfer *via* the hopping mechanism.[137,138] Based on this, Huang *et al.* designed PCN-226 linked by redox-active metalloporphyrins and Zr cations.[136] The Zr cations showed strong affinity with carboxyl-functionalized metalloporphyrins due to the hard soft acid base theory, confirming the stability of PCN-226. Importantly, the as-fabricated Zr-chains could significantly enhance the high chemical and redox stability and significantly modulate the packing of the redox active-sites to improve the reaction kinetics, thereby showing obvious ORR activity. Recently, Cao *et al.* developed MOF-supported CoPy through covalent bonds as a composite pyrolysis-free catalyst for ORR, which solves the aggregation and inefficient utilization problems associated with molecular catalysts. The strategy is shown in Fig. 10d, in which Co tetra(imidazolyl)porphyrin 1 was grafted on a Zn-based zeolitic imidazolate framework (ZIF-8) (named 1@ZIF-8).[139] After grafting CoPy 1 on the ZIF-8 MOF, the $4e^-$ ORR performance was significantly enhanced. As shown in Fig. 10e, 1@ZIF-8 showed a high $E_{1/2}$ of 0.79 V, which was much higher than that of CoPy 1 (0.72 V), Co-free hybrid ZIF-8 (0.6 V) and untreated ZIF-8 (0.60 V). Also, the large difference in the ORR activity between 1@ZIF-8 and the Co-free hybrid confirmed that CoPy 1 was the real active site for ORR. Moreover, the grafted CoPy 1 on ZIF-67, which was previously demonstrated as an active MOF for H_2O_2 reduction, also showed enhanced $4e^-$ selectivity. Similarly, to improve the utilization of molecular catalysts, Wu *et al.* reported the covalent linking of Co(III) corrole to a F-graphdiyne (F-GDY) film *via* a facile nucleophilic substitution,[140] in which F-GDY was well-defined and provided a much higher loading of active sites, even compared to graphene and carbon nanotubes. The as-prepared COF-*Co*-Cor catalyst exhibited $4e^-$ ORR activity with $E_{1/2}$ = 0.875 V, which was much higher than that of Pt/C. The immobilization of Co-corrole on the crystalline semiconducting F-GDY had the advantages of both materials to largely enhance the ORR activity compared with other related systems.

Moreover, covalent organic polymers (COPs) are types of porous pyrolysis-free solid polymers consisting of molecular secondary structural units linked by strong covalent interactions,[141] thereby endowing them with large specific

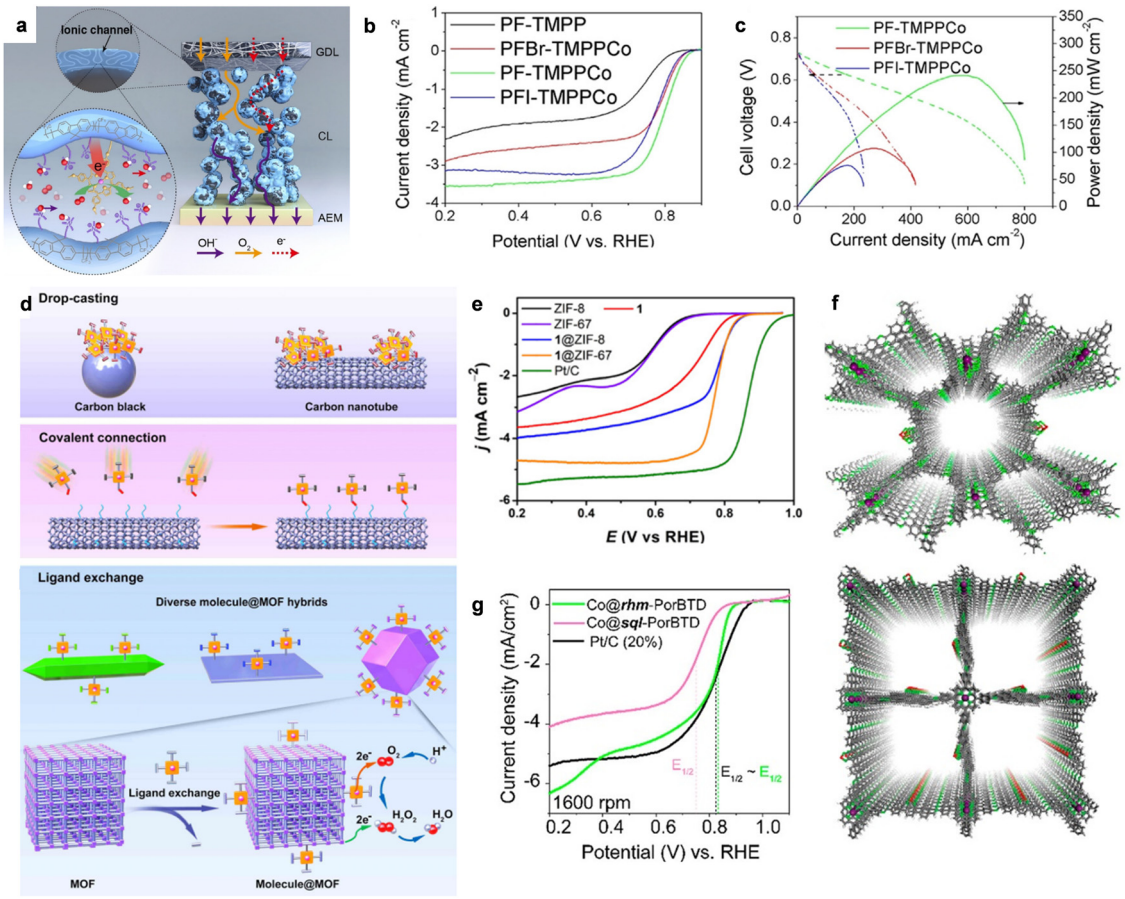

Fig. 10 (a) The advantage of catalyst layer based on homogeneous catalysis using the TMPPCo catalyst. (b) The LSV curves of PF-TMPPCo and the compared catalysts in 0.1 M KOH solution. (c) H_2–O_2 AEMFC performance comparison. Reproduced with permission from ref. 134 Copyright 2020, Wiley-VCH GmbH Publications. (d) The strategies for molecular catalysts to heterogeneous catalysts. (e) The LSV curves of 1-ZIF-67 and the compared catalysts in 0.1 M KOH solution. Reproduced with permission from ref. 139 Copyright 2021, Wiley-VCH GmbH Publications. (f) The top views of the optimized structures of Co@*rhm*-PorBTD (up) and Co@*sql*-PorBTD (down) with eclipsed (AA) structure. (g) ORR LSV curves of Co@*rhm*-PorBTD, Co@*sql*-PorBTD and Pt/C catalysts. Reproduced with permission from ref. 145 Copyright 2023, ACS Publications.

surface areas (up to 4200 $m^2\ g^{-1}$), flexible pore size (~5.0 nm), robust thermal stability (~600 °C) and high charge mobility (~8.1 $cm^2\ V^{-1}\ s^{-1}$).[142] Hence, COPs have also attracted intense interest due to their promising potential applications for oxygen reduction. COPs can not only strongly tailor the incorporation of heteroatoms and locations of active sites, but also supply C/N atoms in the ligands with sufficient flexibility to implant efficient metals into the structure. Additionally, the well-designed COFs with ideal pore size and good stability favor of the electrocatalytic processes in a direct way. However, COPs show mediocre activity compared with the conventional metal-based ORR catalysts due to the constrained electrical conductivity.[143] Combining conductive materials (carbon nanotubes, graphene, *etc.*) or mixing conductive carbon (acetylene black, *etc.*) with COFs is a promising method to improve the conductivity of COP-related ORR catalysts. For instance, Xiang *et al.* reported the preparation of a pyrolysis-free Fe-COF hybrid catalyst self-assembled with graphene *via* van der Waals interaction.[144] The *pf*SAC-Fe hybrids exhibited impressive ORR activity due to the synergistic effect between the active COPs and conductive graphene. Moreover, Echegoyen *et al.* reported the synthesis of two types of Co(II)-porphyrin/[2,1,3]-benzothiadiazole (BTD)-based covalent organic frameworks (Fig. 10f, COFs; Co@*rhm*-PorBTD and Co@*sql*-PorBTD), which showed excellent ORR activity.[145] Moreover, the ORR LSV curves demonstrated that these two COFs showed comparable ORR activity and outperformed the mass activity of Pt/C (20%) by 5.8 times for Co@*rhm*-PorBTD and 1.3 times for Co@*sql*-PorBTD (Fig. 10g).

5.2.3. Metal oxide and related hybrid ORR catalysts. In recent years, transition metal mixed oxides including monometallic oxides, perovskite oxides and spinel oxides have been widely used as ORR catalysts.[5,6,146,147] In particular, perovskite metal oxides have shown great promise for high ORR performance because of their robust crystal structure, high conductivity and rich defects. Recently, versatile perovskite oxides have exhibited high ORR activity.[5,148–151] For instance, Weidner *et al.* reported the preparation of $LaCoO_3$ fibers for ORR by the electrospinning strategy. The as-obtained $LaCoO_3$ fibers exhibited a much higher ORR performance due to the abundant

active sites compared with $LaCoO_3$ powder.[152] Additionally, doping cations or anions is an efficient method to improve the intrinsic activity of catalysts by modulating their electronic structural energy, electronic band structure and oxygen vacancies.[5,153,154] For example, Ramakrishna *et al.* prepared S-doped $CaMnO_3$ (CMO/S) nanotubes by electrospinning and subsequent thermal treatment with S power.[151] The unique microstructure could significantly facilitate the diffusion of oxygen inside and outside the catalyst during the ORR process. Additionally, the incorporation of S could also increase the electric conductivity and vacancy defects in $CaMnO_3$, thereby optimizing the ORR activity of CMO/S. In electrochemical reactions, individual perovskites are relatively limited in regulating the surface electronic states and intermediate adsorption energies. Therefore, the fabrication of perovskite-containing heterostructures with a strong interfacial effect has become one of the effective strategies to enhance the activity of perovskite materials. For instance, Liu *et al.* reported the enhanced ORR performance of hetero-structured SMO_x–SMO synthesized *via* epitaxial growth.[5] The synthesis process is shown in Fig. 11a. It should be noted that SMO_x–SMO and SMO_x–MO with different interfaces were obtained by varying the molar ratio of Sr^{2+} and Mn^{2+}. As shown in Fig. 11b and c, SMO_x–SMO showed superior ORR activity with $E_{1/2}$ = 0.74 V and j of 5.46 mA cm^{-2} at 0.2 V, which was much better than that of SMO_x–MO ($E_{1/2}$ = 0.67 V and j of 5.46 mA cm^{-2} at 0.2 V). According to the simulated results, the epitaxial growth heterojunction of SMO_x–SMO has a more stable thermodynamic structure than non-epitaxial growth of SMO_x–SMO due to the lower formation energy of the former. Also, the positive shift in the Mn band center could enhance the Mn oxidation state, while the partial filling of e_g could significantly optimize the adsorption of intermediate *OH to improve the activity of SMO_x–SMO.

Moreover, the strong scaling relationship of adsorption energy between ORR intermediates gives the minimum theoretical overpotential (~0.3–0.4 V) for a single site, which causes unsatisfactory activity. Hence, constructing a single-site pair-based active site on metal oxides can probably break the limit of the adsorption-energy scale relationship to improve the ORR performance by modulating the spin-state to optimize the adsorption energy. For example, Zou *et al.* developed a Pt-Fe pair by implanting Pt atomic sites on α-Fe_2O_3 (012) facets and the as-fabricated Pt_1–Fe/Fe_2O_3 (012) catalyst delivered a record onset and $E_{1/2}$ of 1.15 and 1.05 V, respectively. The STEM image clearly displayed the individual platinum atoms dispersed on the surface of Fe_2O_3 and the line intensity plot further verified the existence of Pt–Fe pairs. The predicted DFT calculations showed that the d-band of Fe can well match the d-band of Pt, facilitating strong electronic coupling in the Pt–Fe pair. In particular, for Pt_1–Fe/Fe_2O_3 (012), the electron coupling gives Pt a partially occupied d_z^2 near the Fermi level, which can maximize the frontier orbital overlapping. The formed Sigma bonds potentially provide active sites for O_2 adsorption and activation. In addition, considering the transfer of electrons from Fe to Pt, the original completely occupied e_g orbital of high-spin Fe^{3+} became a partially occupied state, which also favored O_2 adsorption. As expected, the ORR polarization curves

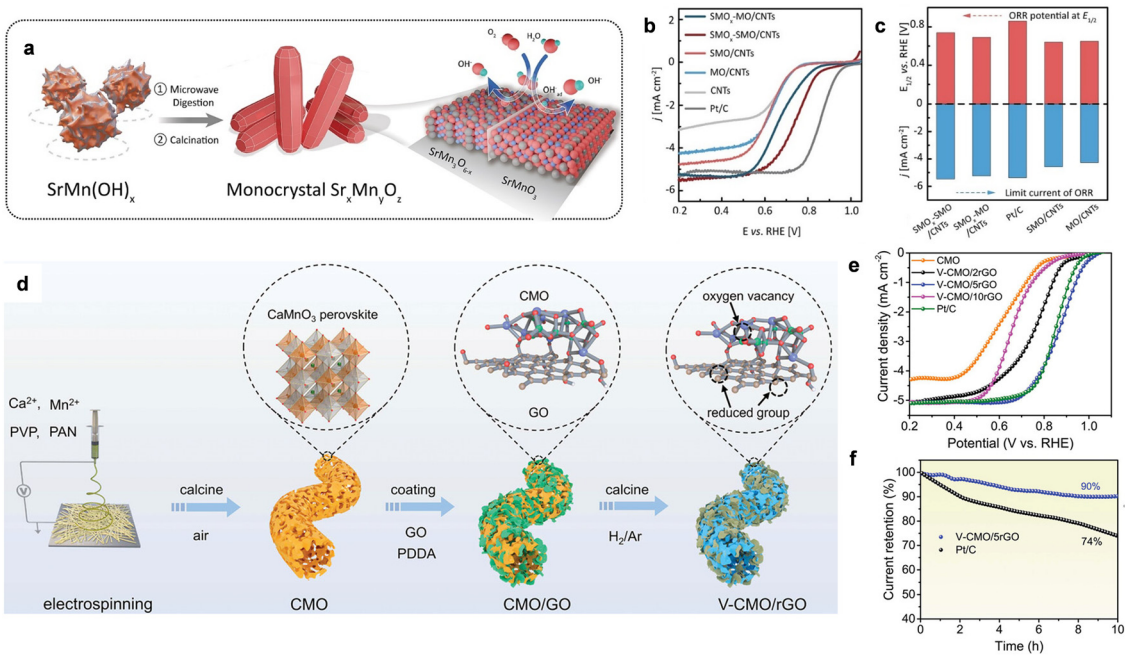

Fig. 11 (a) Th synthesis scheme of SMOx-SMO. (b) The LSV curves of ORR using different catalysts in 0.1 M KOH solution. (c) A comparison of $E_{1/2}$ and the limit current density for the related catalysts. Reproduced with permission from ref. 5 Copyright 2021, Wiley-VCH GmbH Publications. (d) the synthesis process of V-CMO/rGO. (e) ORR polarization curves for V-CMO/rGO and related reference catalysts. (f) The stability tests of V-CMO/rGO and Pt/C catalysts. Reproduced with permission from ref. 155 Copyright 2023, Wiley-VCH GmbH Publications.

showed that Pt_1–Fe/Fe_2O_3 (012) exhibited the highest performance, delivering an extremely high onset potential of 1.15 V, the highest mass activity of 14.9 A mg_{Pt}^{-1} at 0.95 V among the investigated catalysts and robust stability for ORR. The mechanism suggested that the enhanced ORR kinetics was dramatically caused by the facile O_2 activation on the Pt–Fe pair and OH* desorption on the Pt single-site. Thus, the optimized O_2 activation and OH* desorption could overcome the scaling relationships, which could not be optimized on the catalyst per unit point.

Modifying metal oxides with rich oxygen defects has been considered an efficient strategy to design ORR catalysts with high activity. Peng *et al.* developed porous $CaMnO_3$ (CMO) nanofibers modified with rich vacancies and reduced graphene oxide (V-CMO/rGO) as efficient ORR catalysts.[155] V-CMO/rGO was prepared *via* a facile electrospinning method and subsequent electrostatic adsorption of GO with appropriate thermal treatment in air, as shown in Fig. 11d. CMO covered with uniform rGO was obtained by altering the adsorbent amount of GO. Moreover, the final V-CMO/rGO with well-designed 3D framework could not only enhance the exposed active sites, but also increase the electrical conductivity. In particular, the $E_{1/2}$ of V-CMO/5rGO was much higher than that of Pt/C, V-CMO/2rGO and V-CMO/10rGO, as displayed in Fig. 11e. All the CMO catalysts showed superior ORR activity to pure V-CMO because of the highly conductive rGO. The chronoamperometry measurement for the stability test in Fig. 11f verified that V-CMO/5rGO retained better durability than Pt/C. The DFT results demonstrated that CMO as the main active species showed very poor activity for ORR as rGO. Also, Mn was selected as the active site for the $4e^-$ ORR pathway. The excellent performance could stem from the modulation of the oxygen vacancies on the Mn active site, as well as the accelerated electron transfer induced by the uniformly distributed rGO.

6. Summary and perspectives

The importance of the "hydrogen economy" and "ammonia economy" in the modern society cannot be overstated due to their high energy density and carbon neutral nature in the future energy landscape. In the case of AEMFCs, we believe there is still a lot of room for further exploration. Therefore, increasing efforts are a very desirable contribution to this promising area, especially for catalysts. In the past few decades, important research progress has been made in the development of non-precious catalysts for AEMFCs. However, their catalytic activity still does not reach the that of PGMs. For practical application in AEMFCs, the large-scale development of well-structured and cost-effective catalysts is a prerequisite. The future direction of development for catalysts and key challenges for AEMFCs are summarized in Fig. 12, which also properly addresses the comprehensive challenges that require cooperation between industry and academia. It is believed that AEMFC technology will open up a new path for the development of the next generation of energy-conversion devices to meet the growing energy needs of modern society.

6.1. Catalyst screening

Exploring efficient and robust HOR/AOR/ORR non-PGM catalysts that can match or exceed the performance benchmark of

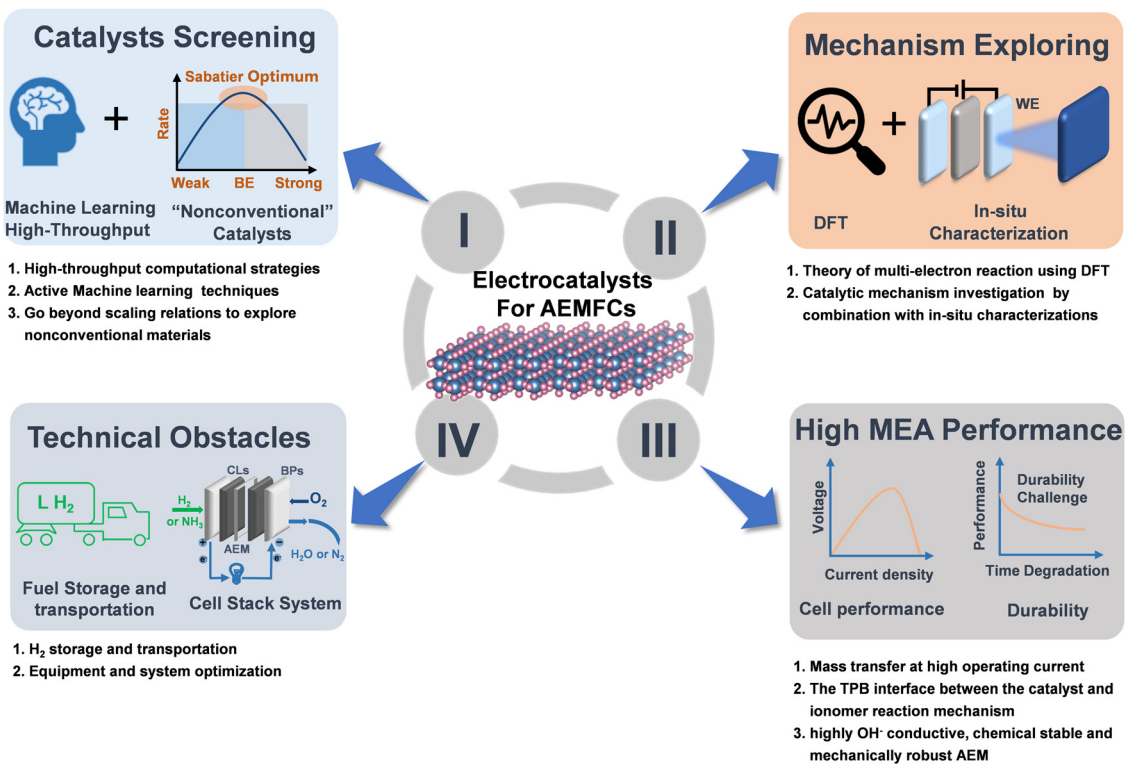

Fig. 12 A schematic of future developments of electrocatalysts for AEMFCs and remaining technological challenges.

PGMs is crucial. Although the excellent performance of TM-based materials has been reported, a great deal of studies still need to be done on this topic. On one hand, exploring new materials through high-throughput computation and active machine learning strategies can greatly accelerate the development in the field.[156,157] On the other hand, the dedicated research for non-traditional materials or structures that inherently outperform the ''standard'' scaling relations can help to design and explore the next generation of efficient catalysts.

6.2. Mechanism exploring

Versatile types of catalysts have been designed for efficient HOR, AOR and ORR; nevertheless, a systematic deep mechanistic understanding of the reactions in alkaline media is still lacking, especially for AOR. Presently, most AOR catalysts are still prepared by trial and error. Alternatively, it is necessary to develop highly active catalysts for potential applications in AEMFCs by combining computational and experimental approaches, especially advanced *in situ* characterization techniques. For example, *in situ*/*operando* XAS, TEM and Raman spectroscopy, are highly required for real-time monitoring of the dynamic evolution process of the catalyst structure. Also, systematic studies can greatly facilitate an in-depth understanding of the catalytic mechanism of catalysts and rational design of more novel low-cost and efficient catalysts.

6.3. High MEA performance

At high current densities, mass transfer is a major limiting factor for RDE and integrated MEA device testing. The RDE test uses a thin CL and low catalyst loading to alleviate the mass transfer problem because thin CLs can facilitate the efficient circulation of the electrolyte. Simultaneously, O_2 diffuses easily from thin CLs. In contrast, thick CLs with a high catalyst loading will cause serious mass transfer problems for reactants or products, resulting in large gaps in performance. Thus, to alleviate the mass transfer problem, thin CLs are directly deposited on the membrane and highly porous conductive substrates. The high hydrophobicity of polymer ionomers may limit the electrolyte proximity to the electrode surface, thereby reducing the cell performance. Hence, it is critical to optimize the three-phase boundary (TPB) of the electrode reaction.

Moreover, the surface functional groups of the catalyst, backbone chains of ionomers, polarity of the solvent, *etc.* can also impact the quality of the catalyst ink and probably cause the catalyst to aggregate on the electrode during the manufacturing of MEAs, thereby blocking the mass transfer channel and degrading the cell performance. In particular, even some stable M–N–C materials showing robust stability in the RDE system are subjected to fast degradation under high-temperature operations. Thus, to alleviate the degradation, robust metal oxides are potentially utilized to stabilize carbon-related catalysts for fuel cells.[38,158] Furthermore, chemically stable, mechanically robust and highly electric conductive AEMs are also urgently required to propel the development of AEMFCs.

6.4. Technical obstacles

Although hydrogen is the most promising fuel due to its simple anodization, its storage and transport are a huge challenge impeding the development of a hydrogen economy. In the case of NH_3, the crossover of ammonia from the anode to cathode *via* AEMs is also a serious challenge. Moreover, the rational design and upgrading of equipment and systems are also highly required to meet the demand of highly safe, low-cost, high-efficiency and facile operability cell stacks under both experimental and practical industry environments.

Conflicts of interest

There are no conflicts to declare.

Acknowledgements

This work was supported by the National Natural Science Foundation of China (No. 22202214, 51825204) and Natural Science Foundation of Liaoning Province-Outstanding Youth Foundation (2022-YQ-02). G. L. thanks the financial support from the New Cornerstone Science Foundation through the XPLORER PRIZE.

References

1 F. Jiao and B. Xu, Electrochemical Ammonia Synthesis and Ammonia Fuel Cells, *Adv. Mater.*, 2019, **31**(31), 1805173.
2 N. M. Adli, H. Zhang, S. Mukherjee and G. Wu, Review-Ammonia Oxidation Electrocatalysis for Hydrogen Generation and Fuel Cells, *J. Electrochem. Soc.*, 2018, **165**(15), J3130.
3 Y. Yang, P. Li, X. Zheng, W. Sun, S. X. Dou, T. Ma and H. Pan, Anion-exchange membrane water electrolyzers and fuel cells, *Chem. Soc. Rev.*, 2022, **51**(23), 9620–9693.
4 Y. Yang, C. R. Peltier, R. Zeng, R. Schimmenti, Q. Li, X. Huang, Z. Yan, G. Potsi, R. Selhorst, X. Lu, W. Xu, M. Tader, A. V. Soudackov, H. Zhang, M. Krumov, E. Murray, P. Xu, J. Hitt, L. Xu, H.-Y. Ko, B. G. Ernst, C. Bundschu, A. Luo, D. Markovich, M. Hu, C. He, H. Wang, J. Fang, R. A. DiStasio, L. F. Kourkoutis, A. Singer, K. J. T. Noonan, L. Xiao, L. Zhuang, B. S. Pivovar, P. Zelenay, E. Herrero, J. M. Feliu, J. Suntivich, E. P. Giannelis, S. Hammes-Schiffer, T. Arias, M. Mavrikakis, T. E. Mallouk, J. D. Brock, D. A. Muller, F. J. DiSalvo, G. W. Coates and H. D. Abruña, Electrocatalysis in Alkaline Media and Alkaline Membrane-Based Energy Technologies, *Chem. Rev.*, 2022, **122**(6), 6117–6321.
5 C. Chen, X.-T. Wang, J.-H. Zhong, J. Liu, G. I. N. Waterhouse and Z.-Q. Liu, Epitaxially Grown Heterostructured $SrMn_3O_{6-x}$-$SrMnO_3$ with High-Valence $Mn^{3+/4+}$ for Improved Oxygen Reduction Catalysis, *Angew. Chem., Int. Ed.*, 2021, **60**(40), 22043–22050.

6 R. Gao, J. Wang, Z.-F. Huang, R. Zhang, W. Wang, L. Pan, J. Zhang, W. Zhu, X. Zhang, C. Shi, J. Lim and J.-J. Zou, Pt/Fe_2O_3 with Pt–Fe pair sites as a catalyst for oxygen reduction with ultralow Pt loading, *Nat. Energy*, 2021, **6**(6), 614–623.

7 A. Han, X. Wang, K. Tang, Z. Zhang, C. Ye, K. Kong, H. Hu, L. Zheng, P. Jiang, C. Zhao, Q. Zhang, D. Wang and Y. Li, An Adjacent Atomic Platinum Site Enables Single-Atom Iron with High Oxygen Reduction Reaction Performance, *Angew. Chem., Int. Ed.*, 2021, **60**(35), 19262–19271.

8 A. Han, Z. Zhang, X. Li, D. Wang and Y. Li, Atomic Thickness Catalysts: Synthesis and Applications, *Small Methods*, 2020, **4**(9), 2000248.

9 A. Han, Z. Zhang, J. Yang, D. Wang and Y. Li, Carbon-Supported Single-Atom Catalysts for Formic Acid Oxidation and Oxygen Reduction Reactions, *Small*, 2021, **17**(16), 2004500.

10 Y. Wang, J. Wu, S. Tang, J. Yang, C. Ye, J. Chen, Y. Lei and D. Wang, Synergistic Fe−Se Atom Pairs as Bifunctional Oxygen Electrocatalysts Boost Low-Temperature Rechargeable Zn-Air Battery, *Angew. Chem., Int. Ed.*, 2023, **62**(15), e202219191.

11 P. Cui, L. Zhao, Y. Long, L. Dai and C. Hu, Carbon-Based Electrocatalysts for Acidic Oxygen Reduction Reaction, *Angew. Chem., Int. Ed.*, 2023, **62**, e202218269.

12 Y. T. Chan, K. Siddharth and M. Shao, Investigation of cubic Pt alloys for ammonia oxidation reaction, *Nano Res.*, 2020, **13**(7), 1920–1927.

13 K. Nakajima, H. Toda, K. Sakata and Y. Nishibayashi, Ruthenium-catalysed oxidative conversion of ammonia into dinitrogen, *Nat. Chem.*, 2019, **11**(8), 702–709.

14 H. Du, Z. Du, T. Wang, B. Li, S. He, K. Wang, L. Xie, W. Ai and W. Huang, Unlocking Interfacial Electron Transfer of Ruthenium Phosphides by Homologous Core–Shell Design toward Efficient Hydrogen Evolution and Oxidation, *Adv. Mater.*, 2022, **34**(37), 2204624.

15 T. Zhao, M. Li, D. Xiao, X. Yang, Q. Li, L. An, Z. Deng, T. Shen, M. Gong, Y. Chen, G. Wang, X. Zhao, L. Xiao, X. Yang, L. Li and D. Wang, Pseudo-Pt Monolayer for Robust Hydrogen Oxidation, *J. Am. Chem. Soc.*, 2023, **145**, 4088–4097.

16 Y. Zhou, Z. Xie, J. Jiang, J. Wang, X. Song, Q. He, W. Ding and Z. Wei, Lattice-confined Ru clusters with high CO tolerance and activity for the hydrogen oxidation reaction, *Nat. Catal.*, 2020, **3**(5), 454–462.

17 S. Zhu, X. Qin, F. Xiao, S. Yang, Y. Xu, Z. Tan, J. Li, J. Yan, Q. Chen, M. Chen and M. Shao, The role of ruthenium in improving the kinetics of hydrogen oxidation and evolution reactions of platinum, *Nat. Catal.*, 2021, **4**(8), 711–718.

18 J. Mao, C.-T. He, J. Pei, Y. Liu, J. Li, W. Chen, D. He, D. Wang and Y. Li, Isolated Ni Atoms Dispersed on Ru Nanosheets: High-Performance Electrocatalysts toward Hydrogen Oxidation Reaction, *Nano Lett.*, 2020, **20**(5), 3442–3448.

19 W. Sheng, Z. Zhuang, M. Gao, J. Zheng, J. G. Chen and Y. Yan, Correlating hydrogen oxidation and evolution activity on platinum at different pH with measured hydrogen binding energy, *Nat. Commun.*, 2015, **6**(1), 5848.

20 W. Sheng, H. A. Gasteiger and Y. Shao-Horn, Hydrogen Oxidation and Evolution Reaction Kinetics on Platinum: Acid vs Alkaline Electrolytes, *J. Electrochem. Soc.*, 2010, **157**(11), B1529.

21 Y. Duan, X.-L. Zhang, F.-Y. Gao, Y. Kong, Y. Duan, X.-T. Yang, X.-X. Yu, Y.-R. Wang, S. Qin, Z. Chen, R. Wu, P.-P. Yang, X.-S. Zheng, J.-F. Zhu, M.-R. Gao, T.-B. Lu, Z.-Y. Yu and S.-H. Yu, Interfacial Engineering of Ni/V_2O_3 Heterostructure Catalyst for Boosting Hydrogen Oxidation Reaction in Alkaline Electrolytes, *Angew. Chem., Int. Ed.*, 2023, **62**(10), e202217275.

22 W. Ni, A. Krammer, C.-S. Hsu, H. M. Chen, A. Schüler and X. Hu, Ni_3N as an Active Hydrogen Oxidation Reaction Catalyst in Alkaline Medium, *Angew. Chem., Int. Ed.*, 2019, **58**(22), 7445–7449.

23 W. Ni, T. Wang, F. Héroguel, A. Krammer, S. Lee, L. Yao, A. Schüler, J. S. Luterbacher, Y. Yan and X. Hu, An efficient nickel hydrogen oxidation catalyst for hydroxide exchange membrane fuel cells, *Nat. Mater.*, 2022, **21**(7), 804–810.

24 M. Wang, H. Yang, J. Shi, Y. Chen, Y. Zhou, L. Wang, S. Di, X. Zhao, J. Zhong, T. Cheng, W. Zhou and Y. Li, Alloying Nickel with Molybdenum Significantly Accelerates Alkaline Hydrogen Electrocatalysis, *Angew. Chem., Int. Ed.*, 2021, **60**(11), 5771–5777.

25 F. Yang, X. Bao, P. Li, X. Wang, G. Cheng, S. Chen and W. Luo, Boosting Hydrogen Oxidation Activity of Ni in Alkaline Media through Oxygen-Vacancy-Rich CeO_2/Ni Heterostructures, *Angew. Chem., Int. Ed.*, 2019, **58**(40), 14179–14183.

26 T. B. Ferriday and P. H. Middleton, Alkaline fuel cell technology - A review, *Int. J. Hydrogen Energy*, 2021, **46**(35), 18489–18510.

27 W. E. Mustain, M. Chatenet, M. Page and Y. S. Kim, Durability challenges of anion exchange membrane fuel cells, *Energy Environ. Sci.*, 2020, **13**(9), 2805–2838.

28 J. Zhang, W. Zhu, T. Huang, C. Zheng, Y. Pei, G. Shen, Z. Nie, D. Xiao, Y. Yin and M. D. Guiver, Recent Insights on Catalyst Layers for Anion Exchange Membrane Fuel Cells, *Adv. Sci.*, 2021, **8**(15), 2100284.

29 A. Serov, I. V. Zenyuk, C. G. Arges and M. Chatenet, Hot topics in alkaline exchange membrane fuel cells, *J. Power Sources*, 2018, **375**, 149–157.

30 D. R. Dekel, Review of cell performance in anion exchange membrane fuel cells, *J. Power Sources*, 2018, **375**, 158–169.

31 S. F. Yin, B. Q. Xu, X. P. Zhou and C. T. Au, A mini-review on ammonia decomposition catalysts for on-site generation of hydrogen for fuel cell applications, *Appl. Catal., A*, 2004, **277**(1), 1–9.

32 Q. Ma, R. Peng, Y. Lin, J. Gao and G. Meng, A high-performance ammonia-fueled solid oxide fuel cell, *J. Power Sources*, 2006, **161**(1), 95–98.

33 Y. Aoki, T. Yamaguchi, S. Kobayashi, D. Kowalski, C. Zhu and H. Habazaki, High-Efficiency Direct Ammonia Fuel Cells Based on $BaZr_{0.1}Ce_{0.7}Y_{0.2}O_{3-\delta}$/Pd Oxide-Metal Junctions, *Glob. Chall.*, 2018, **2**(1), 1700088.

34 O. Siddiqui and I. Dincer, Experimental investigation and assessment of direct ammonia fuel cells utilizing alkaline molten and solid electrolytes, *Energy*, 2019, **169**, 914–923.
35 R. Rossi, W. Yang, E. Zikmund, D. Pant and B. E. Logan, In situ biofilm removal from air cathodes in microbial fuel cells treating domestic wastewater, *Bioresour. Technol.*, 2018, **265**, 200–206.
36 Y. Guo, J. Wang, S. Shinde, X. Wang, Y. Li, Y. Dai, J. Ren, P. Zhang and X. Liu, Simultaneous wastewater treatment and energy harvesting in microbial fuel cells: an update on the biocatalysts, *RSC Adv.*, 2020, **10**(43), 25874–25887.
37 Y. Zhao, B. P. Setzler, J. Wang, J. Nash, T. Wang, B. Xu and Y. Yan, An Efficient Direct Ammonia Fuel Cell for Affordable Carbon-Neutral Transportation, *Joule*, 2019, **3**(10), 2472–2484.
38 Y. Li, H. S. Pillai, T. Wang, S. Hwang, Y. Zhao, Z. Qiao, Q. Mu, S. Karakalos, M. Chen, J. Yang, D. Su, H. Xin, Y. Yan and G. Wu, High-performance ammonia oxidation catalysts for anion-exchange membrane direct ammonia fuel cells, *Energy Environ. Sci.*, 2021, **14**(3), 1449–1460.
39 R. Lan and S. Tao, Direct Ammonia Alkaline Anion-Exchange Membrane Fuel Cells, *Electrochem. Solid State Lett.*, 2010, **13**(8), B83.
40 E. J. Cairns, E. L. Simons and A. D. Tevebaugh, Ammonia–Oxygen Fuel Cell, *Nature*, 1968, **217**(5130), 780–781.
41 T. Hejze, J. O. Besenhard, K. Kordesch, M. Cifrain and R. R. Aronsson, Current status of combined systems using alkaline fuel cells and ammonia as a hydrogen carrier, *J. Power Sources*, 2008, **176**(2), 490–493.
42 J. Yang, H. Muroyama, T. Matsui and K. Eguchi, Development of a direct ammonia-fueled molten hydroxide fuel cell, *J. Power Sources*, 2014, **245**, 277–282.
43 L. Su, D. Gong, Y. Jin, D. Wu and W. Luo, Recent advances in alkaline hydrogen oxidation reaction, *J. Energy Chem.*, 2022, **66**, 107–122.
44 T. Tang, L. Ding, Z.-C. Yao, H.-R. Pan, J.-S. Hu and L.-J. Wan, Synergistic Electrocatalysts for Alkaline Hydrogen Oxidation and Evolution Reactions, *Adv. Funct. Mater.*, 2022, **32**(2), 2107479.
45 X. Tian, P. Zhao and W. Sheng, Hydrogen Evolution and Oxidation: Mechanistic Studies and Material Advances, *Adv. Mater.*, 2019, **31**(31), 1808066.
46 F. Yang, X. Tian, W. Luo and L. Feng, Alkaline hydrogen oxidation reaction on Ni-based electrocatalysts: From mechanistic study to material development, *Coord. Chem. Rev.*, 2023, **478**, 214980.
47 J. Durst, C. Simon, F. Hasché and H. A. Gasteiger, Hydrogen Oxidation and Evolution Reaction Kinetics on Carbon Supported Pt, Ir, Rh, and Pd Electrocatalysts in Acidic Media, *J. Electrochem. Soc.*, 2015, **162**(1), F190.
48 J. Durst, A. Siebel, C. Simon, F. Hasché, J. Herranz and H. A. Gasteiger, New insights into the electrochemical hydrogen oxidation and evolution reaction mechanism, *Energy Environ. Sci.*, 2014, **7**(7), 2255–2260.
49 E. S. Davydova, S. Mukerjee, F. Jaouen and D. R. Dekel, Electrocatalysts for Hydrogen Oxidation Reaction in Alkaline Electrolytes, *ACS Catal.*, 2018, **8**(7), 6665–6690.
50 Z. Zhuang, S. A. Giles, J. Zheng, G. R. Jenness, S. Caratzoulas, D. G. Vlachos and Y. Yan, Nickel supported on nitrogen-doped carbon nanotubes as hydrogen oxidation reaction catalyst in alkaline electrolyte, *Nat. Commun.*, 2016, **7**(1), 10141.
51 B. P. Setzler, Z. Zhuang, J. A. Wittkopf and Y. Yan, Activity targets for nanostructured platinum-group-metal-free catalysts in hydroxide exchange membrane fuel cells, *Nat. Nanotechnol.*, 2016, **11**(12), 1020–1025.
52 F. Chen, J. Ren, F. Cheng, D. Cao, M. Qiao, B. Wu and N. Zheng, Mo-Decorated Ni_3N Nanostructures for Alkaline Polymer Electrolyte Fuel Cells, *ACS Appl. Nano Mater.*, 2021, **4**(11), 11473–11479.
53 X. Zhao, X. Li, L. An, K. Iputera, J. Zhu, P. Gao, R.-S. Liu, Z. Peng, J. Yang and D. Wang, Nitrogen-inserted nickel nanosheets with controlled orbital hybridization and strain fields for boosted hydrogen oxidation in alkaline electrolytes, *Energy Environ. Sci.*, 2022, **15**(3), 1234–1242.
54 X. Zhao, X. Li, L. An, L. Zheng, J. Yang and D. Wang, Controlling the Valence-Electron Arrangement of Nickel Active Centers for Efficient Hydrogen Oxidation Electrocatalysis, *Angew. Chem., Int. Ed.*, 2022, **61**(32), e202206588.
55 H. Kim, H. Park, D. S. Tran and S.-K. Kim, Facile fabrication of amorphous NiMo catalysts for alkaline hydrogen oxidation reaction, *J. Ind. Eng. Chem.*, 2021, **94**, 309–316.
56 D. Salmazo, M. F. Juarez, A. G. Oshchepkov, O. V. Cherstiouk, A. Bonnefont, S. A. Shermukhamedov, R. R. Nazmutdinov, W. Schmickler and E. R. Savinova, On the feasibility of bifunctional hydrogen oxidation on Ni and NiCu surfaces, *Electrochim. Acta*, 2019, **305**, 452–458.
57 O. V. Cherstiouk, P. A. Simonov, A. G. Oshchepkov, V. I. Zaikovskii, T. Y. Kardash, A. Bonnefont, V. N. Parmon and E. R. Savinova, Electrocatalysis of the hydrogen oxidation reaction on carbon-supported bimetallic NiCu particles prepared by an improved wet chemical synthesis, *J. Electroanal. Chem.*, 2016, **783**, 146–151.
58 A. Roy, M. R. Talarposhti, S. J. Normile and I. V. Zenyuk, De Andrade, V.; Artyushkova, K.; Serov, A.; Atanassov, P., Nickel–copper supported on a carbon black hydrogen oxidation catalyst integrated into an anion-exchange membrane fuel cell, *Sustainable Energy Fuels*, 2018, **2**(10), 2268–2275.
59 M. H. Tang, C. Hahn, A. J. Klobuchar, J. W. D. Ng, J. Wellendorff, T. Bligaard and T. F. Jaramillo, Nickel–silver alloy electrocatalysts for hydrogen evolution and oxidation in an alkaline electrolyte, *Phys. Chem. Chem. Phys.*, 2014, **16**(36), 19250–19257.
60 Y. Duan, Z.-Y. Yu, L. Yang, L.-R. Zheng, C.-T. Zhang, X.-T. Yang, F.-Y. Gao, X.-L. Zhang, X. Yu, R. Liu, H.-H. Ding, C. Gu, X.-S. Zheng, L. Shi, J. Jiang, J.-F. Zhu, M.-R. Gao and S.-H. Yu, Bimetallic nickel-molybdenum/tungsten nanoalloys for high-efficiency hydrogen oxidation catalysis in alkaline electrolytes, *Nat. Commun.*, 2020, **11**(1), 4789.
61 D. Strmcnik, M. Uchimura, C. Wang, R. Subbaraman, N. Danilovic, D. van der Vliet, A. P. Paulikas, V. R. Stamenkovic and N. M. Markovic, Improving the

hydrogen oxidation reaction rate by promotion of hydroxyl adsorption, *Nat. Chem.*, 2013, **5**(4), 300–306.

62 S. Sahoo, D. R. Dekel, R. Maric and S. P. Alpay, Atomistic Insights into the Hydrogen Oxidation Reaction of Palladium-Ceria Bifunctional Catalysts for Anion-Exchange Membrane Fuel Cells, *ACS Catal.*, 2021, **11**(5), 2561–2571.

63 Y. Yang, X. Sun, G. Han, X. Liu, X. Zhang, Y. Sun, M. Zhang, Z. Cao and Y. Sun, Enhanced Electrocatalytic Hydrogen Oxidation on Ni/NiO/C Derived from a Nickel-Based Metal–Organic Framework, *Angew. Chem., Int. Ed.*, 2019, **58**(31), 10644–10649.

64 S. Deng, X. Liu, T. Huang, T. Zhao, Y. Lu, J. Cheng, T. Shen, J. Liang and D. Wang, MoO_2 modulated electrocatalytic properties of Ni: investigate from hydrogen oxidation reaction to hydrogen evolution reaction, *Electrochim. Acta*, 2019, **324**, 134892.

65 W. Ji, C. Zhan, D. Li, Y. Xu, Y. Zhang, L. Wang, L. Liu, Y. Wang, W. Chen, H. Geng and X. Huang, Phase and interface engineering of nickel carbide nanobranches for efficient hydrogen oxidation catalysis, *J. Mater. Chem. A*, 2021, **9**(46), 26323–26329.

66 F. Song, W. Li, J. Yang, G. Han, P. Liao and Y. Sun, Interfacing nickel nitride and nickel boosts both electrocatalytic hydrogen evolution and oxidation reactions, *Nat. Commun.*, 2018, **9**(1), 4531.

67 L. Su, D. Gong, N. Yao, Y. Li, Z. Li and W. Luo, Modification of the Intermediate Binding Energies on Ni/Ni_3N Heterostructure for Enhanced Alkaline Hydrogen Oxidation Reaction, *Adv. Funct. Mater.*, 2021, **31**(49), 2106156.

68 F. Yang, P. Han, N. Yao, G. Cheng, S. Chen and W. Luo, Inter-regulated d-band centers of the Ni_3B/Ni heterostructure for boosting hydrogen electrooxidation in alkaline media, *Chem. Sci.*, 2020, **11**(44), 12118–12123.

69 P. Xie, Y. Yao, Z. Huang, Z. Liu, J. Zhang, T. Li, G. Wang, R. Shahbazian-Yassar, L. Hu and C. Wang, Highly efficient decomposition of ammonia using high-entropy alloy catalysts, *Nat. Commun.*, 2019, **10**(1), 4011.

70 H. Tabassum, S. Mukherjee, J. Chen, D. Holiharimanana, S. Karakalos, X. Yang, S. Hwang, T. Zhang, B. Lu, M. Chen, Z. Tang, E. A. Kyriakidou, Q. Ge and G. Wu, Hydrogen generation via ammonia decomposition on highly efficient and stable Ru-free catalysts: approaching complete conversion at 450 °C, *Energy Environ. Sci.*, 2022, **15**(10), 4190–4200.

71 K. Nagaoka, T. Eboshi, Y. Takeishi, R. Tasaki, K. Honda, K. Imamura and K. Sato, Carbon-free H_2 production from ammonia triggered at room temperature with an acidic $RuO_2//\gamma\text{-}Al_2O_3$ catalyst, *Sci. Adv.*, 2017, **3**(4), e1602747.

72 S. Giddey, S. P. S. Badwal, C. Munnings and M. Dolan, Ammonia as a Renewable Energy Transportation Media. *ACS Sustainable*, *Chem. Eng.*, 2017, **5**(11), 10231–10239.

73 M. F. Ezzat and I. Dincer, Comparative assessments of two integrated systems with/without fuel cells utilizing liquefied ammonia as a fuel for vehicular applications, *Int. J. Hydrogen Energy*, 2018, **43**(9), 4597–4608.

74 H. G. Oswin and M. Salomon, THE ANODIC OXIDATION OF AMMONIA AT PLATINUM BLACK ELECTRODES IN AQUEOUS KOH ELECTROLYTE, *Can. J. Chem.*, 1963, **41**(7), 1686–1694.

75 H. Gerischer and A. Mauerer, Untersuchungen Zur anodischen Oxidation von Ammoniak an Platin-Elektroden, *J. Electroanal. Chem. Interfacial Electrochem.*, 1970, **25**(3), 421–433.

76 D. Skachkov, C. Venkateswara Rao and Y. Ishikawa, Combined First-Principles Molecular Dynamics/Density Functional Theory Study of Ammonia Electrooxidation on Pt(100) Electrode, *J. Phys. Chem. C*, 2013, **117**(48), 25451–25466.

77 L. A. Diaz and G. G. Botte, Mathematical modeling of ammonia electrooxidation kinetics in a Polycrystalline Pt rotating disk electrode, *Electrochim. Acta*, 2015, **179**, 519–528.

78 F. J. Vidal-Iglesias, J. Solla-Gullón, J. M. Pérez and A. Aldaz, Evidence by SERS of azide anion participation in ammonia electrooxidation in alkaline medium on nanostructured Pt electrodes, *Electrochem. Commun.*, 2006, **8**(1), 102–106.

79 F. J. Vidal-Iglesias, J. Solla-Gullón, J. M. Feliu, H. Baltruschat and A. Aldaz, DEMS study of ammonia oxidation on platinum basal planes, *J. Electroanal. Chem.*, 2006, **588**(2), 331–338.

80 J. F. E. Gootzen, A. H. Wonders, W. Visscher, R. A. van Santen and J. A. R. van Veen, A DEMS and cyclic voltammetry study of NH_3 oxidation on platinized platinum, *Electrochim. Acta*, 1998, **43**(12), 1851–1861.

81 A. C. A. de Vooys, M. T. M. Koper, R. A. van Santen and J. A. R. van Veen, The role of adsorbates in the electrochemical oxidation of ammonia on noble and transition metal electrodes, *J. Electroanal. Chem.*, 2001, **506**(2), 127–137.

82 T. Matsui, S. Suzuki, Y. Katayama, K. Yamauchi, T. Okanishi, H. Muroyama and K. Eguchi, In Situ Attenuated Total Reflection Infrared Spectroscopy on Electrochemical Ammonia Oxidation over Pt Electrode in Alkaline Aqueous Solutions, *Langmuir*, 2015, **31**(42), 11717–11723.

83 J. A. Herron, P. Ferrin and M. Mavrikakis, Electrocatalytic Oxidation of Ammonia on Transition-Metal Surfaces: A First-Principles Study, *J. Phys. Chem. C*, 2015, **119**(26), 14692–14701.

84 M. D. Zott, P. Garrido-Barros and J. C. Peters, Electrocatalytic Ammonia Oxidation Mediated by a Polypyridyl Iron Catalyst, *ACS Catal.*, 2019, **9**(11), 10101–10108.

85 F. Habibzadeh, S. L. Miller, T. W. Hamann and M. R. Smith, Homogeneous electrocatalytic oxidation of ammonia to N_2 under mild conditions, *Proc. Natl. Acad. Sci. U. S. A.*, 2019, **116**(8), 2849–2853.

86 P. Bhattacharya, Z. M. Heiden, G. M. Chambers, S. I. Johnson, R. M. Bullock and M. T. Mock, Catalytic Ammonia Oxidation to Dinitrogen by Hydrogen Atom Abstraction, *Angew. Chem., Int. Ed.*, 2019, **58**(34), 11618–11624.

87 P. L. Dunn, B. J. Cook, S. I. Johnson, A. M. Appel and R. M. Bullock, Oxidation of Ammonia with Molecular Complexes, *J. Am. Chem. Soc.*, 2020, **142**(42), 17845–17858.

88 Y. Aoki, T. Yamaguchi, S. Kobayashi, D. Kowalski, C. Zhu and H. Habazaki, High-Efficiency Direct Ammonia Fuel

Cells Based on $BaZr_{0.1}Ce_{0.7}Y_{0.2}O_{3-\delta}$/Pd Oxide-Metal Junctions, *Glob. Chall.*, 2018, **2**(1), 1700088.

89 H. S. Pillai and H. Xin, New Insights into Electrochemical Ammonia Oxidation on Pt(100) from First Principles, *Ind. Eng. Chem. Res.*, 2019, **58**(25), 10819–10828.

90 Y. Li, X. Li, H. S. Pillai, J. Lattimer, N. Mohd Adli, S. Karakalos, M. Chen, L. Guo, H. Xu, J. Yang, D. Su, H. Xin and G. Wu, Ternary PtIrNi Catalysts for Efficient Electrochemical Ammonia Oxidation, *ACS Catal.*, 2020, **10**(7), 3945–3957.

91 K. Siddharth, Y. Chan, L. Wang and M. Shao, Ammonia electro-oxidation reaction: Recent development in mechanistic understanding and electrocatalyst design, *Curr. Opin. Electrochem.*, 2018, **9**, 151–157.

92 S. Johnston, B. H. R. Suryanto and D. R. MacFarlane, Electro-oxidation of ammonia on electrochemically roughened platinum electrodes, *Electrochim. Acta*, 2019, **297**, 778–783.

93 Y.-J. Shih, Y.-H. Huang and C. P. Huang, In-situ electrochemical formation of nickel oxyhydroxide (NiOOH) on metallic nickel foam electrode for the direct oxidation of ammonia in aqueous solution, *Electrochim. Acta*, 2018, **281**, 410–419.

94 A. Kapałka, A. Cally, S. Neodo, C. Comninellis, M. Wächter and K. M. Udert, Electrochemical behavior of ammonia at $Ni/Ni(OH)_2$ electrode, *Electrochem. Commun.*, 2010, **12**(1), 18–21.

95 W. Xu, D. Du, R. Lan, J. Humphreys, D. N. Miller, M. Walker, Z. Wu, J. T. S. Irvine and S. Tao, Electrodeposited NiCu bimetal on carbon paper as stable non-noble anode for efficient electrooxidation of ammonia, *Appl. Catal., B*, 2018, **237**, 1101–1109.

96 W. Xu, R. Lan, D. Du, J. Humphreys, M. Walker, Z. Wu, H. Wang and S. Tao, Directly growing hierarchical nickel-copper hydroxide nanowires on carbon fibre cloth for efficient electrooxidation of ammonia, *Appl. Catal., B*, 2017, **218**, 470–479.

97 M. Zhang, P. Zou, G. Jeerh, S. Chen, J. Shields, H. Wang and S. Tao, Electricity Generation from Ammonia in Landfill Leachate by an Alkaline Membrane Fuel Cell Based on Precious-Metal-Free Electrodes. *ACS Sustainable*, *Chem. Eng.*, 2020, **8**(34), 12817–12824.

98 A. Kulkarni, S. Siahrostami, A. Patel and J. K. Nørskov, Understanding Catalytic Activity Trends in the Oxygen Reduction Reaction, *Chem. Rev.*, 2018, **118**(5), 2302–2312.

99 S. Dey, B. Mondal, S. Chatterjee, A. Rana, S. Amanullah and A. Dey, Molecular electrocatalysts for the oxygen reduction reaction, *Nat. Rev. Chem.*, 2017, **1**(12), 0098.

100 X. Shi, S. Back, T. M. Gill, S. Siahrostami and X. Zheng, Electrochemical Synthesis of H_2O_2 by Two-Electron Water Oxidation Reaction, *Chem*, 2021, **7**(1), 38–63.

101 Y. Jiang, P. Ni, C. Chen, Y. Lu, P. Yang, B. Kong, A. Fisher and X. Wang, Selective Electrochemical H2O2 Production through Two-Electron Oxygen Electrochemistry, *Adv. Energy Mater.*, 2018, **8**(31), 1801909.

102 X. Zhang, Y. Xia, C. Xia and H. Wang, Insights into Practical-Scale Electrochemical H_2O_2 Synthesis, *Trends Chem.*, 2020, **2**(10), 942–953.

103 L. Lin, N. Miao, G. G. Wallace, J. Chen and D. A. Allwood, Engineering Carbon Materials for Electrochemical Oxygen Reduction Reactions, *Adv. Energy Mater.*, 2021, **11**(32), 2100695.

104 J. Greeley, I. E. L. Stephens, A. S. Bondarenko, T. P. Johansson, H. A. Hansen, T. F. Jaramillo, J. Rossmeisl, I. Chorkendorff and J. K. Nørskov, Alloys of platinum and early transition metals as oxygen reduction electrocatalysts, *Nat. Chem.*, 2009, **1**(7), 552–556.

105 H.-Y. Su, Y. Gorlin, I. C. Man, F. Calle-Vallejo, J. K. Nørskov, T. F. Jaramillo and J. Rossmeisl, Identifying active surface phases for metal oxide electrocatalysts: a study of manganese oxide bifunctional catalysts for oxygen reduction and water oxidation catalysis, *Phys. Chem. Chem. Phys.*, 2012, **14**(40), 14010–14022.

106 D. F. Abbott, S. Mukerjee, V. Petrykin, Z. Bastl, N. B. Halck, J. Rossmeisl and P. Krtil, Oxygen reduction on nanocrystalline ruthenia – local structure effects, *RSC Adv.*, 2015, **5**(2), 1235–1243.

107 M. Lehtimäki, H. Hoffmannová, O. Boytsova, Z. Bastl, M. Busch, N. B. Halck, J. Rossmeisl and P. Krtil, Targeted design of α-MnO_2 based catalysts for oxygen reduction, *Electrochim. Acta*, 2016, **191**, 452–461.

108 G. A. Tritsaris, J. K. Nørskov and J. Rossmeisl, Trends in oxygen reduction and methanol activation on transition metal chalcogenides, *Electrochim. Acta*, 2011, **56**(27), 9783–9788.

109 A. Han, W. Sun, X. Wan, D. Cai, X. Wang, F. Li, J. Shui and D. Wang, Construction of Co_4 Atomic Clusters to Enable Fe-N_4 Motifs with Highly Active and Durable Oxygen Reduction Performance, *Angew. Chem., Int. Ed.*, 2023, **62**, e202303185.

110 J. W. F. To, J. W. D. Ng, S. Siahrostami, A. L. Koh, Y. Lee, Z. Chen, K. D. Fong, S. Chen, J. He, W.-G. Bae, J. Wilcox, H. Y. Jeong, K. Kim, F. Studt, J. K. Nørskov, T. F. Jaramillo and Z. Bao, High-performance oxygen reduction and evolution carbon catalysis: From mechanistic studies to device integration, *Nano Res.*, 2017, **10**(4), 1163–1177.

111 X. Ge, A. Sumboja, D. Wuu, T. An, B. Li, F. W. T. Goh, T. S. A. Hor, Y. Zong and Z. Liu, Oxygen Reduction in Alkaline Media: From Mechanisms to Recent Advances of Catalysts, *ACS Catal.*, 2015, **5**(8), 4643–4667.

112 F. Abild-Pedersen, J. Greeley, F. Studt, J. Rossmeisl, T. R. Munter, P. G. Moses, E. Skúlason, T. Bligaard and J. K. Nørskov, Scaling Properties of Adsorption Energies for Hydrogen-Containing Molecules on Transition-Metal Surfaces, *Phys. Rev. Lett.*, 2007, **99**(1), 016105.

113 V. Viswanathan, H. A. Hansen, J. Rossmeisl and J. K. Nørskov, Universality in Oxygen Reduction Electrocatalysis on Metal Surfaces, *ACS Catal.*, 2012, **2**(8), 1654–1660.

114 S. Guerin, B. E. Hayden, D. Pletcher, M. E. Rendall and J.-P. Suchsland, A Combinatorial Approach to the Study of Particle Size Effects on Supported Electrocatalysts: Oxygen Reduction on Gold, *J. Comb. Chem.*, 2006, **8**(5), 679–686.

115 K. J. J. Mayrhofer, B. B. Blizanac, M. Arenz, V. R. Stamenkovic, P. N. Ross and N. M. Markovic, The Impact of Geometric and Surface Electronic Properties of Pt-Catalysts on the Particle Size Effect in Electrocatalysis, *J. Phys. Chem. B*, 2005, **109**(30), 14433–14440.

116 L. Jiang, A. Hsu, D. Chu and R. Chen, Size-Dependent Activity of Palladium Nanoparticles for Oxygen Electroreduction in Alkaline Solutions, *J. Electrochem. Soc.*, 2009, **156**(5), B643.
117 R. Jasinski and A. New, Fuel Cell Cathode Catalyst, *Nature*, 1964, **201**(4925), 1212–1213.
118 S. Gupta, D. Tryk, I. Bae, W. Aldred and E. Yeager, Heat-treated polyacrylonitrile-based catalysts for oxygen electroreduction, *J. Appl. Electrochem.*, 1989, **19**(1), 19–27.
119 K. Liu, J. Fu, Y. Lin, T. Luo, G. Ni, H. Li, Z. Lin and M. Liu, Insights into the activity of single-atom Fe-N-C catalysts for oxygen reduction reaction, *Nat. Commun.*, 2022, **13**(1), 2075.
120 L. Peng, J. Yang, Y. Yang, F. Qian, Q. Wang, D. Sun-Waterhouse, L. Shang, T. Zhang and G. I. N. Waterhouse, Mesopore-Rich Fe–N–C Catalyst with FeN_4–O–NC Single-Atom Sites Delivers Remarkable Oxygen Reduction Reaction Performance in Alkaline Media, *Adv. Mater.*, 2022, **34**(29), 2202544.
121 Y. Wang, X. Zheng and D. Wang, Design concept for electrocatalysts, *Nano Res.*, 2022, **15**(3), 1730–1752.
122 E. Luo, Y. Chu, J. Liu, Z. Shi, S. Zhu, L. Gong, J. Ge, C. H. Choi, C. Liu and W. Xing, Pyrolyzed M–Nx catalysts for oxygen reduction reaction: progress and prospects, *Energy Environ. Sci.*, 2021, **14**(4), 2158–2185.
123 H. Adabi, A. Shakouri, N. Ul Hassan, J. R. Varcoe, B. Zulevi, A. Serov, J. R. Regalbuto and W. E. Mustain, High-performing commercial Fe–N–C cathode electrocatalyst for anion-exchange membrane fuel cells, *Nat. Energy*, 2021, **6**(8), 834–843.
124 Y. Yang, X. Xu, P. Sun, H. Xu, L. Yang, X. Zeng, Y. Huang, S. Wang and D. Cao, AgNPs@Fe-N-C oxygen reduction catalysts for anion exchange membrane fuel cells, *Nano Energy*, 2022, **100**, 107466.
125 P. Sun, Z. Qiao, S. Wang, D. Li, X. Liu, Q. Zhang, L. Zheng, Z. Zhuang and D. Cao, Atomically Dispersed Zn-Pyrrolic-N4 Cathode Catalysts for Hydrogen Fuel Cells, *Angew. Chem., Int. Ed.*, 2023, **62**(6), e202216041.
126 J. H. Zagal, Metallophthalocyanines as catalysts in electrochemical reactions, *Coord. Chem. Rev.*, 1992, **119**, 89–136.
127 Y.-M. Zhao, G.-Q. Yu, F.-F. Wang, P.-J. Wei and J.-G. Liu, Bioinspired Transition-Metal Complexes as Electrocatalysts for the Oxygen Reduction Reaction, *Chem. – Eur. J.*, 2019, **25**(15), 3726–3739.
128 J. S. Shpilman, A. Friedman, N. Zion, N. Levy, D. T. Major and L. Elbaz, Combined Experimental and Theoretical Study of Cobalt Corroles as Catalysts for Oxygen Reduction Reaction, *J. Phys. Chem. C*, 2019, **123**(50), 30129–30136.
129 C. W. Machan, Advances in the Molecular Catalysis of Dioxygen Reduction, *ACS Catal.*, 2020, **10**(4), 2640–2655.
130 M. L. Pegis, C. F. Wise, D. J. Martin and J. M. Mayer, Oxygen Reduction by Homogeneous Molecular Catalysts and Electrocatalysts, *Chem. Rev.*, 2018, **118**(5), 2340–2391.
131 J. Wang, S. Dou and X. Wang, Structural tuning of heterogeneous molecular catalysts for electrochemical energy conversion, *Sci. Adv.*, 2021, **7**(13), eabf3989.
132 K. Chen, K. Liu, P. An, H. Li, Y. Lin, J. Hu, C. Jia, J. Fu, H. Li, H. Liu, Z. Lin, W. Li, J. Li, Y.-R. Lu, T.-S. Chan, N. Zhang and M. Liu, Iron phthalocyanine with coordination induced electronic localization to boost oxygen reduction reaction, *Nat. Commun.*, 2020, **11**(1), 4173.
133 A. Friedman, M. Mizrahi, N. Levy, N. Zion, M. Zachman and L. Elbaz, Application of Molecular Catalysts for the Oxygen Reduction Reaction in Alkaline Fuel Cells, *ACS Appl. Mater. Interfaces*, 2021, **13**(49), 58532–58538.
134 R. Ren, X. Wang, H. Chen, H. A. Miller, I. Salam, J. R. Varcoe, L. Wu, Y. Chen, H.-G. Liao, E. Liu, F. Bartoli, F. Vizza, Q. Jia and Q. He, Reshaping the Cathodic Catalyst Layer for Anion Exchange Membrane Fuel Cells: From Heterogeneous Catalysis to Homogeneous Catalysis, *Angew. Chem., Int. Ed.*, 2021, **60**(8), 4049–4054.
135 H. Zhong, K. H. Ly, M. Wang, Y. Krupskaya, X. Han, J. Zhang, J. Zhang, V. Kataev, B. Büchner, I. M. Weidinger, S. Kaskel, P. Liu, M. Chen, R. Dong and X. Feng, A Phthalocyanine-Based Layered Two-Dimensional Conjugated Metal–Organic Framework as a Highly Efficient Electrocatalyst for the Oxygen Reduction Reaction, *Angew. Chem., Int. Ed.*, 2019, **58**(31), 10677–10682.
136 M. O. Cichocka, Z. Liang, D. Feng, S. Back, S. Siahrostami, X. Wang, L. Samperisi, Y. Sun, H. Xu, N. Hedin, H. Zheng, X. Zou, H.-C. Zhou and Z. Huang, A Porphyrinic Zirconium Metal–Organic Framework for Oxygen Reduction Reaction: Tailoring the Spacing between Active-Sites through Chain-Based Inorganic Building Units, *J. Am. Chem. Soc.*, 2020, **142**(36), 15386–15395.
137 S. R. Ahrenholtz, C. C. Epley and A. J. Morris, Solvothermal Preparation of an Electrocatalytic Metalloporphyrin MOF Thin Film and its Redox Hopping Charge-Transfer Mechanism, *J. Am. Chem. Soc.*, 2014, **136**(6), 2464–2472.
138 I. Liberman, R. Shimoni, R. Ifraemov, I. Rozenberg, C. Singh and I. Hod, Active-Site Modulation in an Fe-Porphyrin-Based Metal–Organic Framework through Ligand Axial Coordination: Accelerating Electrocatalysis and Charge-Transport Kinetics, *J. Am. Chem. Soc.*, 2020, **142**(4), 1933–1940.
139 Z. Liang, H. Guo, G. Zhou, K. Guo, B. Wang, H. Lei, W. Zhang, H. Zheng, U.-P. Apfel and R. Cao, Metal–Organic-Framework-Supported Molecular Electrocatalysis for the Oxygen Reduction Reaction, *Angew. Chem., Int. Ed.*, 2021, **60**(15), 8472–8476.
140 J. Zeng, T. Yang, H. Xu, W. Yu, D. Wang, J. Li, Y. Feng, J. Lu, K. P. Loh and J. Wu, Cobalt(III) corrole-tethered semiconducting graphdiyne film for efficient electrocatalysis of oxygen reduction reaction, *Mater. Today Chem.*, 2022, **25**, 100932.
141 N. Kornienko, Y. Zhao, C. S. Kley, C. Zhu, D. Kim, S. Lin, C. J. Chang, O. M. Yaghi and P. Yang, Metal–Organic Frameworks for Electrocatalytic Reduction of Carbon Dioxide, *J. Am. Chem. Soc.*, 2015, **137**(44), 14129–14135.
142 A. P. Côté, A. I. Benin, N. W. Ockwig, M. O'Keeffe, A. J. Matzger and O. M. Yaghi, Porous, Crystalline, Covalent Organic Frameworks, *Science*, 2005, **310**(5751), 1166–1170.
143 X. Cui, S. Lei, A. C. Wang, L. Gao, Q. Zhang, Y. Yang and Z. Lin, Emerging covalent organic frameworks tailored

materials for electrocatalysis, *Nano Energy*, 2020, **70**, 104525.

144 P. Peng, L. Shi, F. Huo, C. Mi, X. Wu, S. Zhang and Z. Xiang, A pyrolysis-free path toward superiorly catalytic nitrogen-coordinated single atom, *Sci. Adv.*, 2019, **5**(8), eaaw2322.

145 S. Bhunia, A. Peña-Duarte, H. Li, H. Li, M. F. Sanad, P. Saha, M. A. Addicoat, K. Sasaki, T. A. Strom, M. J. Yacamán, C. R. Cabrera, R. Seshadri, S. Bhattacharya, J.-L. Brédas and L. Echegoyen, [2,1,3]-Benzothiadiazole-Spaced Co-Porphyrin-Based Covalent Organic Frameworks for O_2 Reduction, *ACS Nano*, 2023, **17**(4), 3492–3505.

146 N. Heller-Ling, M. Prestat, J. L. Gautier, J. F. Koenig, G. Poillerat and P. Chartier, Oxygen electroreduction mechanism at thin $Ni_xCo_{3-x}O_4$ spinel films in a double channel electrode flow cell (DCEFC), *Electrochim. Acta*, 1997, **42**(2), 197–202.

147 Z. Zhuang, Y. Li, R. Yu, L. Xia, J. Yang, Z. Lang, J. Zhu, J. Huang, J. Wang, Y. Wang, L. Fan, J. Wu, Y. Zhao, D. Wang and Y. Li, Reversely trapping atoms from a perovskite surface for high-performance and durable fuel cell cathodes, *Nat. Catal.*, 2022, **5**(4), 300–310.

148 J. Suntivich, H. A. Gasteiger, N. Yabuuchi, H. Nakanishi, J. B. Goodenough and Y. Shao-Horn, Design principles for oxygen-reduction activity on perovskite oxide catalysts for fuel cells and metal–air batteries, *Nat. Chem.*, 2011, **3**(7), 546–550.

149 Z. Li, L. Lv, J. Wang, X. Ao, Y. Ruan, D. Zha, G. Hong, Q. Wu, Y. Lan, C. Wang, J. Jiang and M. Liu, Engineering phosphorus-doped $LaFeO_{3-\delta}$ perovskite oxide as robust bifunctional oxygen electrocatalysts in alkaline solutions, *Nano Energy*, 2018, **47**, 199–209.

150 S. Zhai, H. Xie, P. Cui, D. Guan, J. Wang, S. Zhao, B. Chen, Y. Song, Z. Shao and M. Ni, A combined ionic Lewis acid descriptor and machine-learning approach to prediction of efficient oxygen reduction electrodes for ceramic fuel cells, *Nat. Energy*, 2022, **7**(9), 866–875.

151 S. Peng, X. Han, L. Li, S. Chou, D. Ji, H. Huang, Y. Du, J. Liu and S. Ramakrishna, Electronic and Defective Engineering of Electrospun $CaMnO_3$ Nanotubes for Enhanced Oxygen Electrocatalysis in Rechargeable Zinc–Air Batteries, *Adv. Energy Mater.*, 2018, **8**(22), 1800612.

152 J. Shim, K. J. Lopez, H. J. Sun, G. Park, J. C. An, S. Eom, S. Shimpalee and J. W. Weidner, Preparation and characterization of electrospun $LaCoO_3$ fibers for oxygen reduction and evolution in rechargeable Zn–air batteries, *J. Appl. Electrochem.*, 2015, **45**(9), 1005–1012.

153 X. Sun, Y. Guo, C. Wu and Y. Xie, The Hydric Effect in Inorganic Nanomaterials for Nanoelectronics and Energy Applications, *Adv. Mater.*, 2015, **27**(26), 3850–3867.

154 A. Han, X. Zhou, X. Wang, S. Liu, Q. Xiong, Q. Zhang, L. Gu, Z. Zhuang, W. Zhang, F. Li, D. Wang, L.-J. Li and Y. Li, One-step synthesis of single-site vanadium substitution in 1T-WS_2 monolayers for enhanced hydrogen evolution catalysis, *Nat. Commun.*, 2021, **12**(1), 709.

155 H. Huang, A. Huang, D. Liu, W. Han, C.-H. Kuo, H.-Y. Chen, L. Li, H. Pan and S. Peng, Tailoring Oxygen Reduction Reaction Kinetics on Perovskite Oxides via Oxygen Vacancies for Low-Temperature and Knittable Zinc-Air Batteries, *Adv. Mater.*, 2023, 2303109.

156 M. Zhong, K. Tran, Y. Min, C. Wang, Z. Wang, C.-T. Dinh, P. De Luna, Z. Yu, A. S. Rasouli, P. Brodersen, S. Sun, O. Voznyy, C.-S. Tan, M. Askerka, F. Che, M. Liu, A. Seifitokaldani, Y. Pang, S.-C. Lo, A. Ip, Z. Ulissi and E. H. Sargent, Accelerated discovery of CO_2 electrocatalysts using active machine learning, *Nature*, 2020, **581**(7807), 178–183.

157 Z. W. Ulissi, M. T. Tang, J. Xiao, X. Liu, D. A. Torelli, M. Karamad, K. Cummins, C. Hahn, N. S. Lewis, T. F. Jaramillo, K. Chan and J. K. Nørskov, Machine-Learning Methods Enable Exhaustive Searches for Active Bimetallic Facets and Reveal Active Site Motifs for CO_2 Reduction, *ACS Catal.*, 2017, **7**(10), 6600–6608.

158 H. Xie, X. Xie, G. Hu, V. Prabhakaran, S. Saha, L. Gonzalez-Lopez, A. H. Phakatkar, M. Hong, M. Wu, R. Shahbazian-Yassar, V. Ramani, M. I. Al-Sheikhly, D.-E. Jiang, Y. Shao and L. Hu, Ta–TiO_x nanoparticles as radical scavengers to improve the durability of Fe–N–C oxygen reduction catalysts, *Nat. Energy*, 2022, **7**(3), 281–289.

159 X.-L. Zhang, S.-J. Hu, Y.-H. Wang, L. Shi, Y. Yang and M.-R. Gao, Plasma-Assisted Synthesis of Metal Nitrides for an Efficient Platinum-Group-Metal-Free Anion-Exchange-Membrane Fuel Cell, *Nano Lett.*, 2023, **23**(1), 107–115.

160 S. Qin, Y. Duan, X.-L. Zhang, L.-R. Zheng, F.-Y. Gao, P.-P. Yang, Z.-Z. Niu, R. Liu, Y. Yang, X.-S. Zheng, J.-F. Zhu and M.-R. Gao, Ternary nickel–tungsten–copper alloy rivals platinum for catalyzing alkaline hydrogen oxidation, *Nat. Commun.*, 2021, **12**(1), 2686.

161 W. Ni, T. Wang, P. A. Schouwink, Y. C. Chuang, H. M. Chen and X. Hu, Efficient Hydrogen Oxidation Catalyzed by Strain-Engineered Nickel Nanoparticles, *Angew. Chem., Int. Ed.*, 2020, **59**(27), 10797–10801.

162 F. Yang, X. Bao, Y. Zhao, X. Wang, G. Cheng and W. Luo, Enhanced HOR catalytic activity of PGM-free catalysts in alkaline media: the electronic effect induced by different heteroatom doped carbon supports, *J. Mater. Chem. A*, 2019, **7**(18), 10936–10941.

163 P. A. Simonov, O. V. Cherstiouk, A. N. Kuznetsov, V. I. Zaikovskii, T. Y. Kardash, A. G. Oshchepkov, A. Bonnefont and E. R. Savinova, Highly active carbon-supported Ni catalyst prepared by nitrate decomposition with a sacrificial agent for the hydrogen oxidation reaction in alkaline medium, *J. Electroanal. Chem.*, 2019, **852**, 113551.

164 G. Wang, W. Li, B. Huang, L. Xiao, J. Lu and L. Zhuang, Exploring the Composition–Activity Relation of Ni–Cu Binary Alloy Electrocatalysts for Hydrogen Oxidation Reaction in Alkaline Media, *ACS Appl. Energy Mater.*, 2019, **2**(5), 3160–3165.

165 Y. Gao, H. Peng, Y. Wang, G. Wang, L. Xiao, J. Lu and L. Zhuang, Improving the Antioxidation Capability of the Ni Catalyst by Carbon Shell Coating for Alkaline Hydrogen Oxidation Reaction, *ACS Appl. Mater. Interfaces*, 2020, **12**(28), 31575–31581.

166 V. Men Truong, J. Richard Tolchard, J. Svendby, M. Manikandan, H. Miller, S. Sunde, H. Yang, R. Dekel and A. Oyarce Barnett, Platinum and Platinum Group Metal-Free Catalysts for Anion Exchange Membrane Fuel Cells, *Energies*, 2020, **13**(3), 582.

167 S. Kabir, K. Lemire, K. Artyushkova, A. Roy, M. Odgaard, D. Schlueter, A. Oshchepkov, A. Bonnefont, E. Savinova, D. C. Sabarirajan, P. Mandal, E. J. Crumlin, V. Zenyuk Iryna, P. Atanassov and A. Serov, Platinum group metal-free NiMo hydrogen oxidation catalysts: high performance and durability in alkaline exchange membrane fuel cells, *J. Mater. Chem. A*, 2017, **5**(46), 24433–24443.

168 S. Gu, W. Sheng, R. Cai, S. M. Alia, S. Song, K. O. Jensen and Y. Yan, An efficient Ag–ionomer interface for hydroxide exchange membrane fuel cells, *Chem. Commun.*, 2013, **49**(2), 131–133.

169 Q. Hu, G. Li, J. Pan, L. Tan, J. Lu and L. Zhuang, Alkaline polymer electrolyte fuel cell with Ni-based anode and Co-based cathode, *Int. J. Hydrogen Energy*, 2013, **38**(36), 16264–16268.

170 Z. Jiang, X. Liu, X.-Z. Liu, S. Huang, Y. Liu, Z.-C. Yao, Y. Zhang, Q.-H. Zhang, L. Gu, L.-R. Zheng, L. Li, J. Zhang, Y. Fan, T. Tang, Z. Zhuang and J.-S. Hu, Interfacial assembly of binary atomic metal-Nx sites for high-performance energy devices, *Nat. Commun.*, 2023, **14**(1), 1822.

171 L. Yang, H. Liu, Z. Qiao, P. Sun, D. Li, R. Jiang, S. Liu, Z. Niu, Y. Zhang, T. Lin, Q. Zhang, L. Gu, S. Wang, D. Cao and Z. Chen, Highly Active and Durable Metal-Free Carbon Catalysts for Anion-Exchange Membrane Fuel Cells, *Adv. Energy Mater.*, 2023, **13**(20), 2204390.

172 Y. Liu, S. Yuan, C. Sun, C. Wang, X. Liu, Z. Lv, R. Liu, Y. Meng, W. Yang, X. Feng and B. Wang, Optimizing Fe-3d Electron Delocalization by Asymmetric Fe–Cu Diatomic Configurations for Efficient Anion Exchange Membrane Fuel Cells, *Adv. Energy Mater.*, 2023, 2302719.

173 Y. Persky, Ł. Kielesiński, S. N. Reddy, N. Zion, A. Friedman, H. C. Honig, B. Koszarna, M. J. Zachman, I. Grinberg, D. T. Gryko and L. Elbaz, Biomimetic Fe–Cu Porphyrrole Aerogel Electrocatalyst for Oxygen Reduction Reaction, *ACS Catal.*, 2023, **13**(16), 11012–11022.

174 J. Y. Jung, H. Jin, M. W. Kim, S. Kim, J.-G. Kim, P. Kim, Y.-E. Sung, S. J. Yoo and N. D. Kim, Atomization driven crystalline nanocarbon based single-atom catalysts for superior oxygen electroreduction, *Appl. Catal., B*, 2023, **323**, 122172.

175 Y. Liu, X. Liu, Z. Lv, R. Liu, L. Li, J. Wang, W. Yang, X. Jiang, X. Feng and B. Wang, Tuning the Spin State of the Iron Center by Bridge-Bonded Fe-O-Ti Ligands for Enhanced Oxygen Reduction, *Angew. Chem., Int. Ed.*, 2022, **61**(21), e202117617.

176 G. Xing, M. Tong, P. Yu, L. Wang, G. Zhang, C. Tian and H. Fu, Reconstruction of Highly Dense Cu$-$$N_4$ Active Sites in Electrocatalytic Oxygen Reduction Characterized by *Operando* Synchrotron Radiation, *Angew. Chem., Int. Ed.*, 2022, **61**(40), e202211098.

177 R. Zeng, Y. Yang, X. Feng, H. Li, L. M. Gibbs, F. J. DiSalvo and H. D. Abruña, Nonprecious transition metal nitrides as efficient oxygen reduction electrocatalysts for alkaline fuel cells, *Sci. Adv.*, 2022, **8**(5), eabj1584.

178 T. Meng, P. Sun, F. Yang, J. Zhu, B. Mao, L. Zheng and M. Cao, Double-atom dealloying-derived Frank partial dislocations in cobalt nanocatalysts boost metal–air batteries and fuel cells, *Proc. Natl. Acad. Sci. U. S. A.*, 2022, **119**(45), e2214089119.

179 K. Kisand, A. Sarapuu, J. C. Douglin, A. Kikas, A. Treshchalov, M. Käärik, H.-M. Piirsoo, P. Paiste, J. Aruväli, J. Leis, V. Kisand, A. Tamm, D. R. Dekel and K. Tammeveski, Templated Nitrogen-, Iron-, and Cobalt-Doped Mesoporous Nanocarbon Derived from an Alkylresorcinol Mixture for Anion-Exchange Membrane Fuel Cell Application, *ACS Catal.*, 2022, **12**(22), 14050–14061.

180 S. Huang, Z. Qiao, P. Sun, K. Qiao, K. Pei, L. Yang, H. Xu, S. Wang, Y. Huang, Y. Yan and D. Cao, The strain induced synergistic catalysis of FeN_4 and MnN_3 dual-site catalysts for oxygen reduction in proton-/anion- exchange membrane fuel cells, *Appl. Catal., B*, 2022, **317**, 121770.

181 B. Yang, X. Li, Q. Cheng, X. Jia, Y. Liu and Z. Xiang, A highly efficient axial coordinated CoN_5 electrocatalyst via pyrolysis-free strategy for alkaline polymer electrolyte fuel cells, *Nano Energy*, 2022, **101**, 107565.

182 P. Sun, K. Qiao, D. Li, X. Liu, H. Liu, L. Yang, H. Xu, Z. Zhuang, Y. Yan and D. Cao, Designing oxygen-doped Fe-N-C oxygen reduction catalysts for proton- and anion-exchange-membrane fuel cells, *Chem. Catal.*, 2022, **2**(10), 2750–2763.

183 J. Feng, R. Cai, E. Magliocca, H. Luo, L. Higgins, G. L. F. Romario, X. Liang, A. Pedersen, Z. Xu, Z. Guo, A. Periasamy, D. Brett, T. S. Miller, S. J. Haigh, B. Mishra and M. M. Titirici, Iron, Nitrogen Co-Doped Carbon Spheres as Low Cost, Scalable Electrocatalysts for the Oxygen Reduction Reaction, *Adv. Funct. Mater.*, 2021, **31**, 46.

184 N. Zion, J. C. Douglin, D. A. Cullen, P. Zelenay, D. R. Dekel and L. Elbaz, Porphyrin Aerogel Catalysts for Oxygen Reduction Reaction in Anion-Exchange Membrane Fuel Cells, *Adv. Funct. Mater.*, 2021, **31**(24), 2100963.

185 H. A. Firouzjaie and W. E. Mustain, Catalytic Advantages, Challenges, and Priorities in Alkaline Membrane Fuel Cells, *ACS Catal.*, 2020, **10**(1), 225–234.

186 X. Peng, T. J. Omasta, E. Magliocca, L. Wang, J. R. Varcoe and W. E. Mustain, Nitrogen-doped Carbon–CoOx Nanohybrids: A Precious Metal Free Cathode that Exceeds 1.0 W cm^{-2} Peak Power and 100 h Life in Anion-Exchange Membrane Fuel Cells, *Angew. Chem., Int. Ed.*, 2019, **58**(4), 1046–1051.